nature physics

Article

https://doi.org/10.1038/s41567-025-03037-x

Obstacles regulate membrane tension propagation to enable localized mechanotransduction

Received: 14 January 2025

Accepted: 19 August 2025

Frederic Català-Castro[1,4,5], **Mayte Bonilla-Quintana**[2,5], **Neus Sanfeliu-Cerdán**[1], **Padmini Rangamani**[2,3,6] ✉ & **Michael Krieg**[1,6] ✉

Forces applied to cellular membranes lead to transient membrane tension gradients. The way membrane tension propagates away from the stimulus site into the membrane reservoir is a key property in cellular adaptation. However, it remains unclear how tension propagation in membranes is regulated and how it depends on the cell type. Here we investigate plasma membrane tension propagation in cultured *Caenorhabditis elegans* mechanosensory neurons. We show that tension propagation travels quickly and is restricted to a particular distance in neurites—projections from the cell body of a neuron. A biophysical model of tension propagation suggests that periodic obstacle density and arrangement play key roles in controlling the propagation of mechanical information. Our experiments show that tension propagation is strongly dependent on the intact actin and microtubule cytoskeleton, whereas membrane lipid properties have a minimal impact. In particular, organization of the α/β-spectrin network and the MEC-2 stomatin condensates in a periodic scaffold acts as barriers to tension propagation, limiting the spread of tension. Our findings suggest that restricting membrane tension propagation in space and time enables precise localized signalling, allowing a single neuron to process mechanical signals in multiple distinct domains and, thus, expanding its computational capacity.

The transmission of mechanical information through the cytoskeleton, organelles and plasma membrane is vital for the organization of cells and mechanotransduction[1,2]. Plasma membrane mechanics are central to how cells respond to external forces, influencing cell shape[3], signalling[4] and metabolism[5]. These mechanical properties are defined by in-plane elasticity, bending rigidity, resistance to flow through membrane viscosity and, through coupling to the underlying cortex, an effective membrane tension[6]. Furthermore, it has been extensively reported that local tension gradients, due to a large membrane reservoir or the fluid character of the lipid bilayer, rapidly relax in metazoan cells[7–12], but may be heterogeneous along the contour of the cell[13–16]. Thus, the presence of such a lipid reservoir implies that the membrane cannot support or store mechanical stresses on timescales longer than its viscous relaxation time, resulting in a constant membrane tension[7]. Due to this, it is believed that a local increase in tension generated by an application of local forces (due to an external tether extrusion[7] or an internal actin protrusion[17]) is rapidly propagated across the entire membrane surface. This idea has placed membrane tension as an effective

---

[1] ICFO—Institut de Ciències Fotòniques, Castelldefels, The Barcelona Institute of Science and Technology, Barcelona, Spain. [2] Department of Mechanical and Aerospace Engineering, University of California San Diego, San Diego, CA, USA. [3] Department of Pharmacology, School of Medicine, University of California San Diego, San Diego, CA, USA. [4] Present address: IMPETUX, Barcelona, Spain. [5] These authors contributed equally: Frederic Català-Castro, Mayte Bonilla-Quintana. [6] These authors jointly supervised this work: Padmini Rangamani, Michael Krieg. ✉e-mail: prangamani@health.ucsd.edu; michael.krieg@icfo.eu

mediator of communication between mechanical events occurring at different locations along the membrane[17,18]. However, the specific details of the propagation of membrane tension appear to be system specific[10,15,18,19]. For example, these views were recently challenged by the observation that membrane tension does not propagate in tissue culture cells, suggesting that the increased tension gradient remains locally confined to regions around the neck of the tether and does not relax for many minutes[15]. Likewise, in bacterial cells, the tension generated during tether pulling did not relax, indicating that the tension of the resting membrane is globally regulated and close to the lytic tension[20]. However, in axons of cultured neurons[18,19], tension was shown to propagate many tens of micrometres.

This raises questions about how tension propagation is regulated along the membrane and what is the corresponding cellular adaptation mechanism to an external force. To provide an insight into these questions, we established optical-tweezers-based membrane nanorheology with a single, time-shared laser source[21–23] to study membrane tension propagation mechanics between a pair of lipid nanotubes extruded from a single axon. We used the well-studied touch receptor neurons (TRNs) of *Caenorhabditis elegans* as a biophysical model for tension propagation in axons. This model system has gained interest in the mechanophysiological regulation of animal behaviour[24–26]. These neurons are important for the animal's response to external forces. Although the exact mechanism of mechanotransduction is still not defined, genes affecting mechanoresponses are known and encode not only proteins of the extracellular matrix[27], microtubules[28], integral and peripheral membrane proteins[29,30], and the cortical cytoskeleton[31] but also the membrane itself[32]. The spectrin cytoskeleton, in particular, has received ample attention and is known to organize associated membrane proteins into periodic clusters[33,34], and is under constitutive mechanical tension[31]. Although the role of the spectrin's mechanical properties in mechanosensation is well known in *C. elegans*[26,31], *Drosophila*[35,36], chicken[37] and mouse[38,39], the consequences of spectrin integrity on the propagation of membrane tension gradients is not understood. Likewise, stomatin homologues such as MEC-2 and STOML3, which contribute to mechanotransduction in the sensory neurons of *C. elegans* and mice[29,40], bind cholesterol[41] and modulate membrane stiffness[40]. Strikingly, MEC-2 forms discrete condensates along the axonal membrane in vivo, arranged at regular intervals of 2–4 μm (ref. 28). However, the functional implications of this periodic organization remain unclear.

To understand the link between the organization of these cellular elements and tension propagation, we combined our experimental results with a theoretical model proposed in refs. 15,18, in which tension propagation is associated with membrane lipid flow, but hindered by cytoskeleton-bound transmembrane proteins. The basic principle of our model is the same as those proposed before[15,18], based on Brinkman flow, which extends the Stokes equation by adding a Darcy-like resistance term, allowing it to model viscous flow through porous media in which both shear stress and permeability effects are significant[42]. Using this formalism, we conducted three-dimensional simulations using finite element methods to compare the effect of membrane elasticity, viscosity and permeability on tension propagation.

Our results suggest that membrane tension is locally confined, and accordingly, we reveal that tension propagation into the axon is limited by obstacles. Because we find that the extent of propagation differs between proprioceptive and touch mechanoreceptor neurons that respond to different modalities, we propose that propagation speed and magnitude is an intrinsic property of the cell type and under tight genetic control.

Results

The active trap

To study how cell membrane mechanics enables tension propagation along the plasma membrane, we began our investigation with the classical tether extrusion experiment[43]. Similar to our previous approach with mechanosensitive proprioceptors[10], we used an optically trapped microsphere as a force probe and formed a contact between the probe and the membrane of isolated TRNs of *C. elegans* (Fig. 1a). On successful non-specific attachment and withdrawal of the microsphere from the neurite, a membrane tether formed that required a constant force to maintain its position, reflecting the underlying baseline (or resting) membrane tension. A rapid retraction of the microsphere leads to an increase in force on the trapped bead, indicating the extension of the lipid nanotube (Extended Data Fig. 1a). After reaching a predefined distance from the neurite, we stopped the movement of the trap and held the probe at a fixed position. Immediately, the tether force rapidly decayed to a static value, which was different from the baseline value on the timescale of our experiment and independent of the initial extrusion velocity and, therefore, independent of the membrane viscosity (Extended Data Fig. 1a), similar to what was observed before[43]. As noted previously, a higher retraction velocity caused an increased force on the microsphere[10], due to the finite viscosity and resulting resistance of the membrane to flow into the tether (Extended Data Fig. 1b)[44,45]. This viscosity-dominated peak increased with velocity up to 120 pN and was suggestive of the maximum tension difference of more than 1 mN m^{-1} generated during pull-out (Extended Data Fig. 1b,c). As the rapid increase in tension during the tether pull-out is not due to fluid drag of the probe with the surrounding medium (Methods), we reasoned that the limited lipid flow into the tether caused this striking tension difference.

When the microsphere is moved again towards the neurite such that the membrane tether is released back into it, the force drops below its resting value, indicating negative tension differentials (Fig. 1b,c). However, the baseline, resting plasma membrane tension recovered within 2–3 s ($F_{\mathrm{rest}} \approx 9$–12 pN), indicating a mechanism that maintains tension homeostasis. The resting force F_{rest} is related to the membrane tension σ_{rest} through the bending rigidity of the membrane κ according to

$$\sigma_{\mathrm{rest}} = \frac{F_{\mathrm{rest}}^2}{8\pi^2\kappa}. \tag{1}$$

Thus, using this simple relation, we can approximate the tension in the membrane by measuring the resting forces on the bead in the trap[43,46].

At high extrusion velocities, we observed spherical instabilities forming within the extruded membrane tube. These instabilities originated near the tether neck and propagated towards the microsphere (Supplementary Video 1 and Extended Data Fig. 1d). Similar dynamics are frequently observed in mechanical instabilities[47]. This instability travelled along the tether, indicative of a gradient in mechanical-tension-driven transport. Interestingly, and in contrast to previous observations[18], the instability never visually propagated to the neuronal process, indicating that the increase in membrane tension was locally confined and hardly propagated into the neurite (Extended Data Fig. 1d). From these results, we concluded that there exists a strong tension difference inside the tether, compared with the resting tension of the axonal membrane far from the tether, which does not, or only incompletely, propagate into the neurite. This difference gives rise to a tension gradient over the length of the tether, which relaxes as lipid flows from the membrane reservoir into the tether. Under a constant tether length, radial expansion driven by lipid transport reflects the classical inverse scaling between the tether force and radius[48].

Active and passive traps

To gain an insight into the mechanism of tension propagation in neurons, we directly measured the extent of tension propagation along the axon to a point perturbation. To do so, we established an optical trapping experiment to simultaneously extrude two membrane

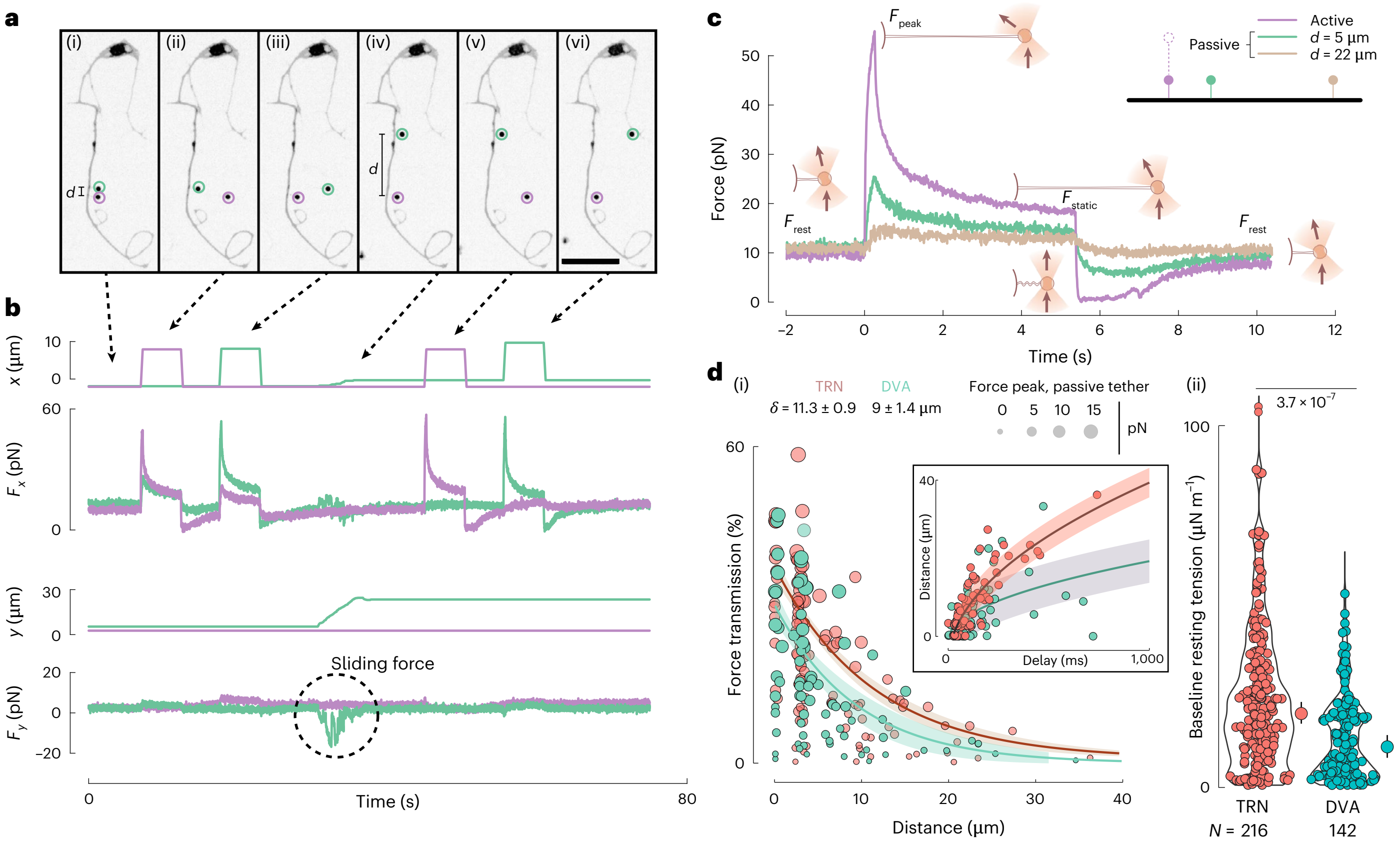

Fig. 1 | A dual-trap assay to measure membrane tension propagation. **a**, Representative image of an isolated TRN with two membrane tethers extruded by two optically trapped microspheres (purple and green circles for active and passive traps, respectively). Scale bar, 20 μm. (i) The two beads are connected to the axonal membrane through the extrusion of a lipid nanotube. (ii) and (iii) Both beads are sequentially pulled at 40 μm s^{-1} to a length of 10 μm, whereas the resting, passive trap records changes in membrane tension at a distance *d*. (iv)–(vi) *d* is increased to record tension propagation under varying separations. **b**, The *x* (top) and *y* (bottom) components of the trap trajectory and force. The sequence of events depicted in **a** are indicated with black arrows. The sliding friction (F_y component) between events (iii) and (iv) is indicated with a dashed circle. **c**, Simultaneous force measurement during trapezoidal pulling routines for the active and passive traps placed at *d* = 5 μm (event (ii) in **a** and **b**) and *d* = 22 μm (event (v) in **a** and **b**). Although a small increase in membrane tension in the passive trap is detected when it is placed close to the active trap, membrane tension at *d* = 22 μm shows no force peak but a slow, second-scale tension increase. The force drop $F_x \to 0$ at $t = 5$ indicates tether buckling on the fast approach of the trap towards the axon. Trap velocity is faster than the ability of the axon to absorb the lipidic material from the tether. Afterwards, tension homeostasis induces tension recovery. The schematic inside the plot graphically illustrates the events and the deflection of the laser due to bead displacement from the trapping centre. Thick arrows indicate the laser direction. **d**, (i) Change in peak membrane tension measured at the passive, lipid nanotube for increasing distances normalized to the active, pulling site, calculated using equation (6). The size of the points corresponds to the absolute transmitted force at the passive tether. The solid line is the exponential fit, with the error band indicating the 95% confidence interval of the fit; *δ* indicates the characteristic length scales derived from the exponential fit; the *P* value = 0.03 is derived from comparing a linear regression on pooled data with interaction term (Methods). The red points indicate values derived from TRNs, and green points, from DVA. The inset shows the tension propagation velocity for the two cell types. The solid line indicates the best fit of $t^{0.5}$ to the data with the 95% confidence interval. (ii) Resting plasma membrane tension of TRN- versus DVA-cultured neurons. The median of the distribution is shown as a circle to the right of the violin, with the vertical bar indicating the 95% confidence interval. The *P* value is derived from a two-sided Kolmogoroff–Smirnoff test. *N* is the number of tether extrusion events.

tethers with a single, time-shared laser source (Fig. 1a, Supplementary Video 2, Extended Data Fig. 2a and Supplementary Text). Similar to our previous time-shared optical tweezers microrheology scheme[23], we split a single laser source at 25 kHz to generate two traps that can be moved independently in two dimensions (Fig. 1a, Extended Data Fig. 2 and Supplementary Text). Due to the interleaved operation of the two traps in the time-shared configuration, we assessed the impact of temporal multiplexing on force measurements. We simulated the bead's response to an external tether force within a periodically switching optical trap, which predicted a systematic deviation, independent of the measured force (Extended Data Fig. 2b and Supplementary Text). This prediction was experimentally validated by comparing tether extrusion events conducted in a continuously active trap versus a time-shared trap. The measured forces in the time-shared configuration were consistently underestimated by a factor of 0.63, which we applied as a correction factor throughout our analysis. Using these two effectively simultaneous optical traps, we extruded a single membrane tether with each of the two traps that were placed in close proximity to each other (Fig. 1a). Then, we actively pulled on the tether in trap 1, and measured the response in the static tether held with trap 2 (Fig. 1b). We alternated this procedure for trap 1 and trap 2 and repeated the extrusion protocol for dual-tether distances of up to 40 μm (Fig. 1c and Supplementary Video 2). As expected, the baseline tension measured in the active and passive traps is indistinguishable, demonstrating that the tension of the unperturbed membrane is homogeneous throughout the neurite (Extended Data Fig. 3a).

In addition to the active trap described above, the passive trap also displayed rich behaviour. At close separations from the active trap (directly opposite to the active trap), we observed a strong reduction in the propagated peak force (Fig. 1c). Only ~40%–50% of the force of the active trap reached the passive trap, even at distances of less than 1 μm. The force propagation velocity from the active to passive tether was very rapid and, in contrast to previous work, exceeded 150 µm s^{-1}. However, the time required to reach the passive trap increased nonlinearly with distance (Fig. 1d, inset), suggesting that the propagation velocity of the mechanical pulse decreases as it travels along the neurite (Extended Data Fig. 3b–e and Methods). We also observed considerable variability in the propagation length scale (Fig. 1d) and velocity (Extended Data Fig. 3e), which may reflect the involvement of distinct propagation mechanisms—such as transmission through the membrane, the cytoskeleton or the viscoelastic cytoplasm.

With increasing distance from the active tether, the peak of the passive trap decreased substantially (Fig. 1d) until it seemed to disappear. At >20 µm of tether separation, the peak was completely buffered. Instead, we observed a slow and steady (almost on the scale of seconds) increase in a plateau value (Fig. 1c, brown curve), suggesting that the membrane behaves as a low-pass filter for mechanical signal transmission—only the slow components get propagated up to 40 µm. This plateau force does not significantly depend on the distance to the active tether (Extended Data Fig. 3f). To calculate the extent of force propagation, we plotted the ratio of the peak force in the passive tether to the peak force in the active tether as a function of the distance x between the two tethers (Fig. 1d) and fitted an exponential decay function $\exp(x) = A\exp(-x/\delta)$ using weighted nonlinear least squares to the absolute peak force of the passive tether (Methods), where δ is the characteristic length scale of the tension propagation and A is the amplitude of the ratio. The weighted exponential (Akaike information criterium (AIC): 854) fitted the data better than a Gaussian (diffusion) kernel (AIC: 860) or a hyperbolic function. Thus, we used an exponential function to quantify tension propagation distances and mechanistically dissect the governing mechanical properties.

We then sought to understand whether tension propagation is different in mechanoreceptor neurons with different functions and turned to DVA proprioceptors. The DVA neuron differs from TRNs in that it contains a single axon, which senses local changes in body bending to coordinate body curvature[10,49]. We previously showed that higher tension gradients during tether extrusion transiently suppress calcium signals in DVA through the two-pore potassium channel K2P TWK-16 (ref. 10). Conversely, tether relaxation and the resulting negative membrane tension gradients initiate local calcium transients that propagate along cultured neurites via the mechanosensitive NOMPC TRP-4 channel[10]. This model, in which a local reduction in membrane tension after the relaxation of the tether (for example, negative tension gradient) activates NOMPC TRP-4 under mechanical compression[50,51] and positive tension—and membrane stretch—opens K2P channels[52], provides a coherent framework for bidirectional mechanosensory tuning[53]. We, thus, speculated that mechanical stresses compartmentalize the axon into dynamic active zones. One requirement of this model is that the spread of mechanical information is limited within the axonal membrane. By applying our dual-tether assay, we found that the resting tether force is lower compared with TRNs (Fig. 1d(ii); $P = 3.7 \times 10^{-7}$, two-sided Kolmogoroff–Smirnoff test) and that the tension remained more confined in DVA and did not propagate far (Fig. 1d(i)) compared with the measurements in TRNs (Fig. 1d, 11.5 versus 9 µm). Intriguingly, we found that the propagation velocity was lower in DVA than in TRNs (Fig. 1d), indicating slower transport of mechanical information along the membranes of proprioceptive neurons. TRNs are known to be exquisitely responsive to high-frequency stimulation above 10 Hz (refs. 54–56), whereas DVA also responds to slower (<1 Hz) proprioceptive cues such as undulatory body motion[10,49]. Thus, the transport mechanics may impose a lower bound on the frequency response, helping neurons selectively respond to different stimulation velocities. Together, this indicates that membrane tension propagated further and faster in TRNs. More generally, our data show that the extent and speed of membrane tension propagation is cell-type specific, which motivated us to dissect the molecular and mechanical mechanisms of tension propagation in neurons.

Membrane tension propagation is restricted by membrane obstacles

Following recent attempts to quantitatively describe tension propagation[15], we assumed that the membrane lipid flow transmits local changes in tension and that cytoskeleton-bound transmembrane proteins, such as cell adhesion molecules, ion channels and membrane–cortex crosslinkers, act as obstacles impeding membrane flow (see the 'Tension propagation model' section). These dynamics are described by

$$\frac{E_\mathrm{m}}{\eta}\nabla^2\sigma = \left(-\nabla^2 + \frac{1}{k}\right)\frac{\partial\sigma}{\partial t}, \qquad (2)$$

where the membrane tension, σ, represents the force per unit length acting on a membrane cross-section. This force counteracts the membrane stretching or compression. The effective area expansion modulus of the cell membrane, E_m, is a material property of the membrane, and it specifies the relationship between the force applied to the membrane and the resulting change in its surface area. η, the two-dimensional membrane viscosity, resists the flow of lipids and other molecules inside the membrane. The Darcy permeability of the obstacles, k, measures the ease with which tension propagates through the membrane (Fig. 2a). We used a cylinder as an idealized geometry for a segment of the axon, and the tethers were represented by attached thinner cylinders (Fig. 2a). As shown in refs. 15,18, we defined the permeability $k = a^2 f(\phi)$ by the obstacle area a and a function of the obstacle density ϕ: $f(\phi) = -(1 + \ln[\phi])/(8\phi)$. This function was derived from the calculation of the mean force required to drag one particle with mean velocity through the background of immobile particles[18]. For typical values of $\phi < 0.3$ (ref. 18), f is a decreasing function of obstacle density. Thus, increased permeability results from a reduced number of obstacles covering the same area, as well as an increase in obstacle size, which can occur due to molecule clustering (Fig. 2b).

Fig. 2 | Theoretical model for tension propagation. a, Schematic of the modelled axon: tension σ generated by pulling the active tether σ_t propagates along the axon. The left inset shows a random distribution of membrane obstacles. The right inset shows a snapshot of the simulation at time 2.25 s. The distance between the tethers is 3 µm and the colour bar represents the tension σ. CAM, cell adhesion molecules. **b**, Top view of the membrane in **a**, showing possible ways to change the permeability k. **c**, Change in membrane tension measured in the passive lipid nanotube for increasing distances normalized to the active, pulling site, with different permeabilities due to randomly distributed obstacles. The size of the circle corresponds to the amount of tension in the passive tether in the simulation ($0 < \sigma \leq 3$ pN µm^{-1} (small), $3 < \sigma \leq 6$ pN µm^{-1} (medium) and $6 < \sigma \leq 9$ pN µm^{-1} (big)). Black represents the control condition. **d**, Lateral view of the axon showing its underlying molecular structure. **e**, Periodic distribution of obstacles along the axon and the corresponding values of k_+ and k_-. The image on the right shows the colour-coded values of k_+ (red) and k_- (blue) along the axon in the simulation. Note that the values are interpolated and follow the underlying triangular mesh. **f**, Change in membrane tension using a periodic configuration for different parameters. Note that k corresponds to the mean value of the permeability along the axon that takes $k_+ = 1.5k$ and $k_- = (3k - k_+)/2$. The grey colour corresponds to the control condition. **g**–**i**, Two-dimensional phase diagram of tension propagation in the presence of periodically arranged obstacles with synergistically varying E_m and η (**g**), E_m and k (**h**) and k and η (**i**). The corresponding parameter values are denoted on the vertical and horizontal axes. The colours represent the extent of tension propagation δ. The exact values of δ are added to the heat map. NaN (black squares) represents conditions for which simulations at certain displacements did not converge. Panels **a**, **b** and **d** created with BioRender.com.

From equation (2), we observed that tension propagation is governed by the parameters E_m, η and k. Hence, we examined the effect of changing these parameters in tension propagation using finite element simulations in a cylindrical geometry (Methods). To quantify the extent of tension propagation, we fitted the same exponential decay model from the experimental data ($A\exp(-x/\delta)$) to the simulation data. However, there was a systematic underestimation of the exponential fit function for large distances between tethers in the simulations. Adding an offset parameter C to the exponential decay (that is, $A\exp(-x/\delta) + C$) resulted in better fittings (for $k = 0.03\ \mu m^2$, the AIC without offset is 42.99 and the AIC with offset is 8.24) and reflects the propagated tension at long distances. Additionally, this offset in the simulations accounts for processes not represented in the model, such as material sources and sinks. When the permeability k is high, there are fewer and/or smaller obstacles in the membrane, allowing it to flow more freely (Fig. 2b). Consequently, the propagation

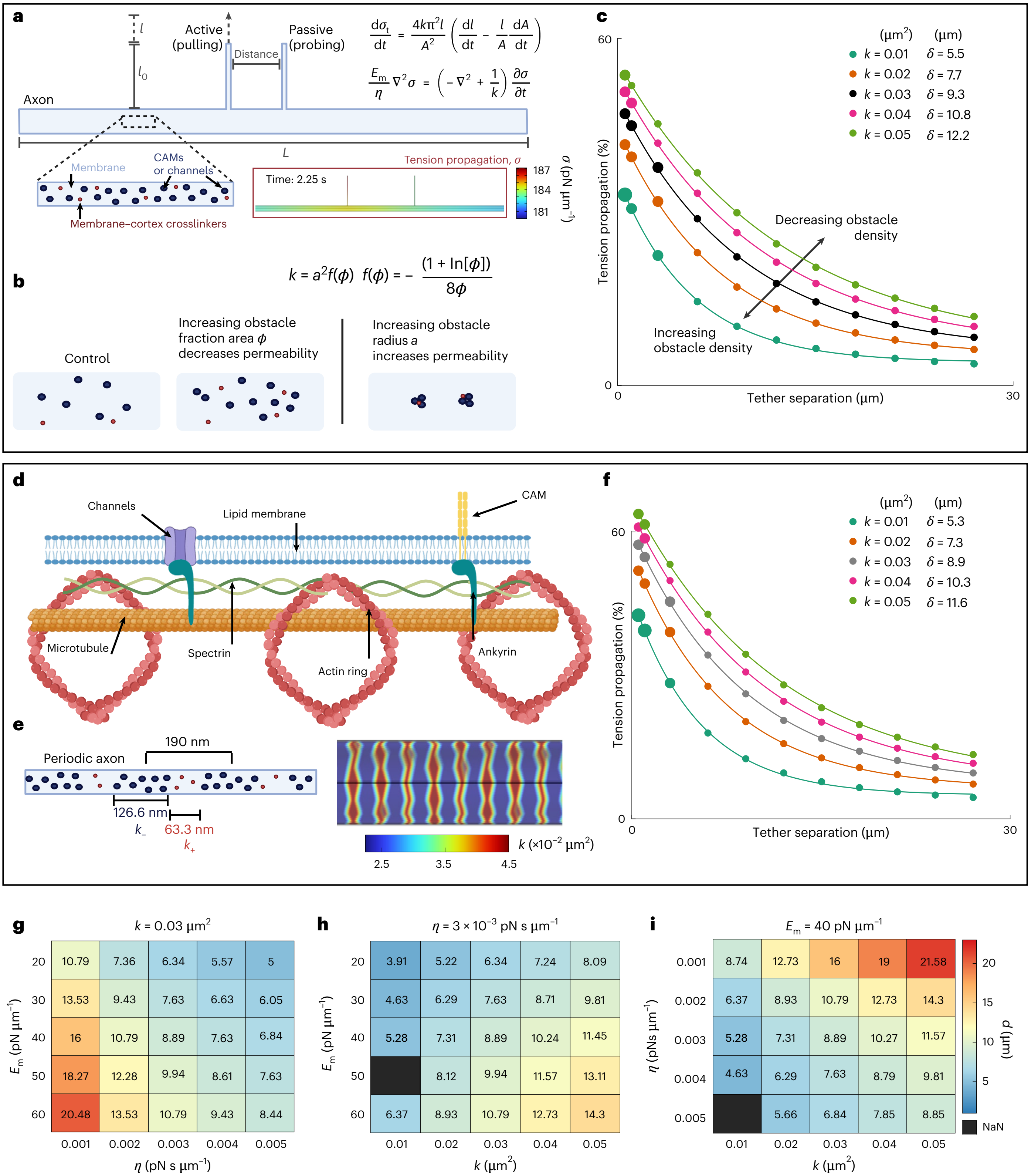

g $k = 0.03\ \mu m^2$

E_m (pN μm^{-1}) \ η (pN s μm^{-1})	0.001	0.002	0.003	0.004	0.005
20	10.79	7.36	6.34	5.57	5
30	13.53	9.43	7.63	6.63	6.05
40	16	10.79	8.89	7.63	6.84
50	18.27	12.28	9.94	8.61	7.63
60	20.48	13.53	10.79	9.43	8.44

h $\eta = 3 \times 10^{-3}$ pN s μm^{-1}

E_m (pN μm^{-1}) \ k (μm^2)	0.01	0.02	0.03	0.04	0.05
20	3.91	5.22	6.34	7.24	8.09
30	4.63	6.29	7.63	8.71	9.81
40	5.28	7.31	8.89	10.24	11.45
50	■	8.12	9.94	11.57	13.11
60	6.37	8.93	10.79	12.73	14.3

i $E_m = 40$ pN μm^{-1}

η (pNs μm^{-1}) \ k (μm^2)	0.01	0.02	0.03	0.04	0.05
0.001	8.74	12.73	16	19	21.58
0.002	6.37	8.93	10.79	12.73	14.3
0.003	5.28	7.31	8.89	10.27	11.57
0.004	4.63	6.29	7.63	8.79	9.81
0.005	■	5.66	6.84	7.85	8.85

https://doi.org/10.1038/s41567-025-03037-x

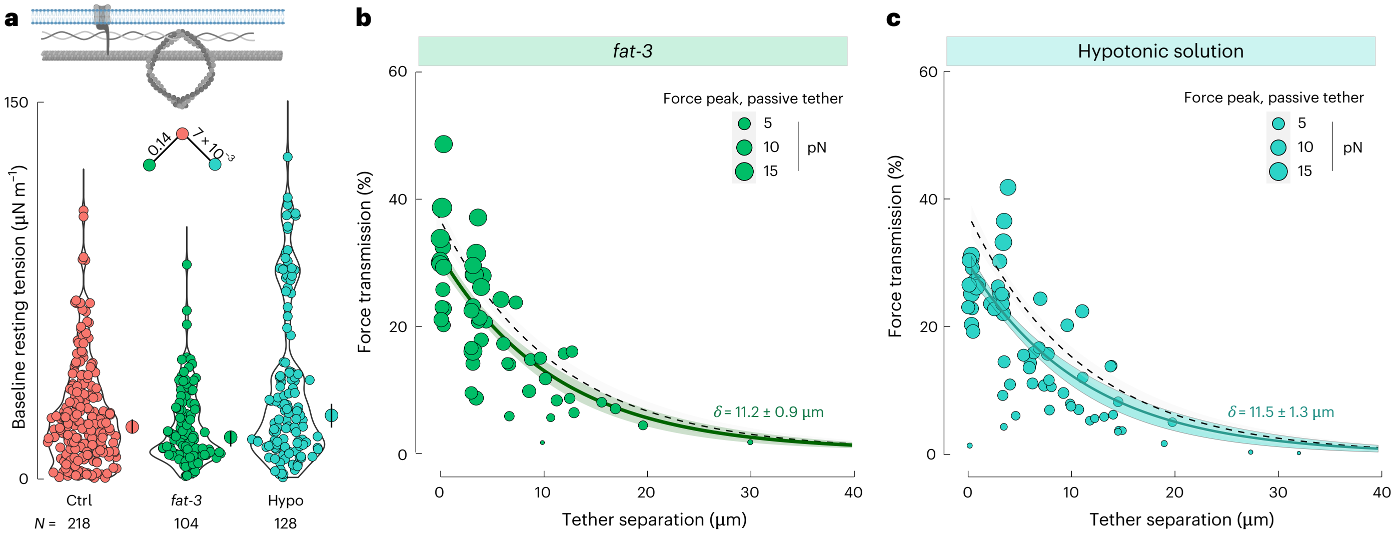

Fig. 3 | Hypotonic shock but not lipid saturation modulates tether forces extruded from neurites. a, Violin plot of the baseline, resting membrane tension during the membrane extrusion for control cells, *fat-3* mutants, that perturb lipid composition, and on cells treated with hypotonic shock. The median is shown as a circle, with the vertical bar indicating the 95% confidence interval next to the violin distribution. *N*, number of measurements. The top schematic highlights the membrane in sky blue. *P* values derived from a two-sided Kolmogoroff–Smirnoff test are shown above the colour-coded combinations. **b**,**c**, Tension propagation in the membrane of mutant cells for *fat-3* (**b**) and cells treated with a hypotonic solution (**c**). The solid lines indicate the fit to an exponential decay; the shaded area indicates the 95% confidence interval of the fit (Methods), and the dotted black line indicates the fit derived from the control data (Fig. 1d). The size of the dots corresponds to the absolute force transmitted to the passive tether. Fit parameter *δ* indicates the characteristic length scale.

of tension increases as the permeability k increases (Fig. 2c and Extended Data Fig. 4a). Because our model also incorporates membrane elasticity, we asked to what extent E_m affects tension propagation. We found that the more elastic the membrane, the greater the tension at the tether, which increases the extent of tension propagation along the axon (Extended Data Fig. 4b). Last, we hypothesized that a higher viscosity hinders the lipid flow of the membrane and, hence, localizes the tension propagation to a smaller region. Indeed, when the viscosity η increases, we observed a decrease in tension propagation (Extended Data Fig. 4c). Together, our simulations suggest a striking dependence of tension propagation on membrane in-plane elasticity, viscosity and obstacle density.

Recent studies have shown that ion channels are organized in a periodic arrangement of obstacles along the axon[34] and dendrites[57] of neurons from various organisms, including *C. elegans*[26]. Our initial model assumes that obstacles are randomly and homogeneously placed in neurites, which may not reflect the physiological organization in neurons. The periodic arrangement is governed by the actin–spectrin cytoskeleton, in which the spectrin tetramers expand ~190 nm and connect adjacent actin rings (Fig. 2d). We introduced this periodic arrangement along the axon by assuming that although ion channels and transmembrane proteins are present along the axonal membrane, they assemble into different clusters, based on experimental observations[34]. Moreover, we assumed that two-thirds of the 190-nm periodic interval is covered by channels and one-third, by smaller obstacles attached to the actin rings (Fig. 2e)[34]. We proposed that permeability k in the zone related to actin rings is higher ($k_+ = 1.5k$) than in the zones covered by channels ($k_- = (3k - k_+)/2$) due to the larger projected area of often multimeric ion channels (for example, Piezo2 (ref. 58)) compared with single-pass transmembrane proteins or G-protein-coupled receptors (Fig. 2e). We varied the parameters and observed that tension propagated less in the periodic control case, that is, using k from the homogeneous control case to calculate k_+ and k_-, than in the homogeneous control case (Fig. 2f). In all cases, the ratio of the passive to active tension peak is higher compared with the random obstacle arrangement. This indicates that a periodic arrangement localized tension, leading to less propagation along the axon. Indeed, our parameter sweep confirmed this assessment even though the parameters show the same tendency as in the homogeneous, randomized organization (Extended Data Fig. 4b–e). A consequence of the periodic arrangement is that tension decays faster with distance, leading to a more confined mechanical tension propagation. Note that the trend is clear for all the fitting results of the length scale and that the random and periodic arrangements are statistically significant for $k = 0.02$, 0.03 and 0.04 µm², and some values of η and E_m (Extended Data Fig. 4a,f,g). Because the simulations are deterministic, the shorter tension propagation in the periodic case is a causal consequence of the change in spatial organization of the obstacles and is highly relevant for the functional outcome of the mechanical properties. Together, our simulations show that periodic obstacles can curb the extent of tension propagation along axonal membranes.

We reasoned that due to the complex nature of membrane–cortex interactions, the model parameters cannot be directly attributed to specific membrane or cytoskeletal components. Instead, tension propagation appears to be governed by multiple synergistically acting parameters. For example, changing the actin organization and membrane–cortex adhesion may disrupt obstacle density but also change the viscosity[3]. To better understand how these parameters jointly influence tension propagation, we performed simulations by varying two parameters simultaneously. Figure 2g–i shows that the tension can propagate further when the parameters are changed simultaneously. For example, in Fig. 2g, decreasing η results in larger tension propagation for any value of E_m, but if E_m is increased, the tension propagates further. This suggests a cooperative effect of both parameters, η and E_m, on tension propagation. Moreover, the degree of tension propagation depends on the ratio η/E_m. Note that in equation (2), this ratio gives the timescale of the dynamics. In summary, we detected a stronger synergistic relationship between the parameters k and η and that the periodic arrangement of obstacles affected the propagation of tension in silico. We next investigated the role of these properties systematically in experiments.

Lipid saturation has little influence on tension propagation

Through atomic-force-microscopy-based tether pulling experiments[45] from the cell body of TRNs, we have previously shown that lipid saturation modifies the viscous properties of the membrane but not the baseline

https://doi.org/10.1038/s41567-025-03037-x

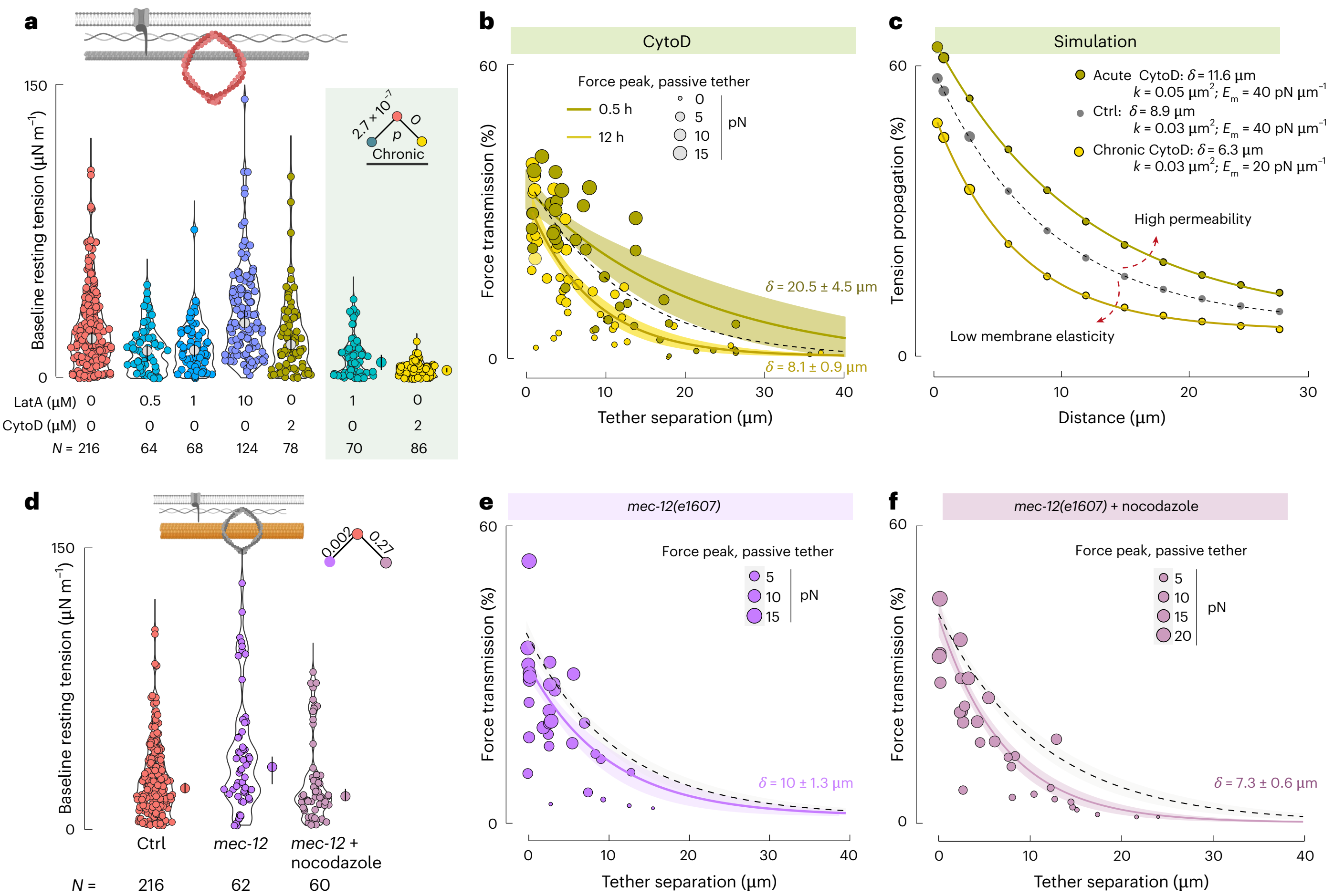

Fig. 4 | Tension propagation is sensitive to F-actin and microtubule network integrity. a, Influence of the F-actin cytoskeleton on baseline, resting membrane tension in cells treated with different concentrations of cytochalasin and latrunculin to perturb the F-actin cytoskeleton. Chronic incubation is performed overnight (12 h). **b**, Tension propagation in cells after acute (green) and chronic (yellow) incubation with CytoD. **c**, Simulation of tension propagation with reduced E_m and increased k compared with the control, describing chronic and acute actin depolymerization. Parameters used for simulation are shown in the figure. The simulation corresponds to the periodic case. Hence, the value of k is used to calculate k_+ and k_- (Extended Data Fig. 4). **d**–**f**, Influence of the microtubule cytoskeleton on static membrane tension (**d**) and tension propagation in the *mec-12* mutant (**e**) and cell treated with nocodazole (**f**). For **a** and **d**, the top schematic highlights the different cytoskeleton elements of interest. The median is indicated as a circle, with a vertical bar indicating the confidence interval of 95%. *N*, number of measurements. *P* values above the colour-coded combinations are derived from a two-sided Kolmogoroff–Smirnoff test (Supplementary Table 1). For **b**, **e** and **f**, the solid lines indicate a fit to an exponential decay and the shaded area indicates the 95% confidence interval of the fit (Methods) and the dotted black line indicates the fit derived from the control data (Fig. 1d). The size of the dots corresponds to the absolute force transmitted to the passive tether. Fit parameter δ indicates the characteristic length scale.

resting tension[32]. Therefore, we asked whether lipid saturation and osmotic effects influence tension propagation along the neurite. *fat-3* mutant neurons with defects in polyunsaturated fatty acid synthesis[32,59] did not have a discernible effect (Fig. 3a,b). However, because our tissue culture medium contained 10% fetal bovine serum, the effect of *fat-3* may be partially confounded by polyunsaturated fatty acids in the medium[60]. Recently, intracellular pressure was shown to influence the rate at which tension propagated along the membrane in HEK293T cell cultures[61]. We also observed that the application of a hypo-osmotic shock significantly increased the tether force ($P = 0.007$). However, we detected no significant difference in tension propagation compared with the wild type (Fig. 3c; $\delta = 11.3$ versus 11.5 μm). Together, these data show that tension propagation is surprisingly robust to subtle changes in the composition of the lipid bilayer and increases with intracellular osmotic pressure. Furthermore, it suggests that tension propagation may be dominated by obstacles in the membrane and cytoskeleton.

Scale of tension propagation is modulated by the cytoskeleton

In our simulations, we treated the membrane and the underlying cytoskeleton as a composite material and assumed that changes in the cytoskeleton affect membrane permeability. This is because transmembrane proteins, which connect to the actin cytoskeleton, can act as obstacles to the flow of lipids in the membrane, as suggested in previous work[62]. Therefore, we measured tension propagation and static tension in four different treatments with latrunculin A (LatA), a pharmacological agent that sequesters actin monomers and is known to interfere with actin polymerization[63], and also cytochalasin D (CytoD), a drug known to depolymerize dynamic actin filaments[64]. At low concentrations of LatA (delivered at 0.5–1 μM acutely, 30-min incubation time), we did not observe an effect on membrane tension (Fig. 4a) or on tension propagation (Fig. 4b and Extended Data Figs. 5 and 6). This is consistent with earlier studies showing that low concentrations of LatA do not disrupt stable actin filaments and do not interfere either with membrane tension extruded from the neuronal cell bodies[31] or with actin ring disassembly in *Drosophila* neurons[65]. In particular, the acute application of 10-μM LatA resulted in an unexpected increase in the baseline resting membrane tension (Fig. 4a) that was accompanied by a significant reduction in tension propagation (Supplementary Table 1). This observation was remarkably different on the acute delivery of 2-μM CytoD, which effectively promoted tension propagation (Fig. 4b),

https://doi.org/10.1038/s41567-025-03037-x

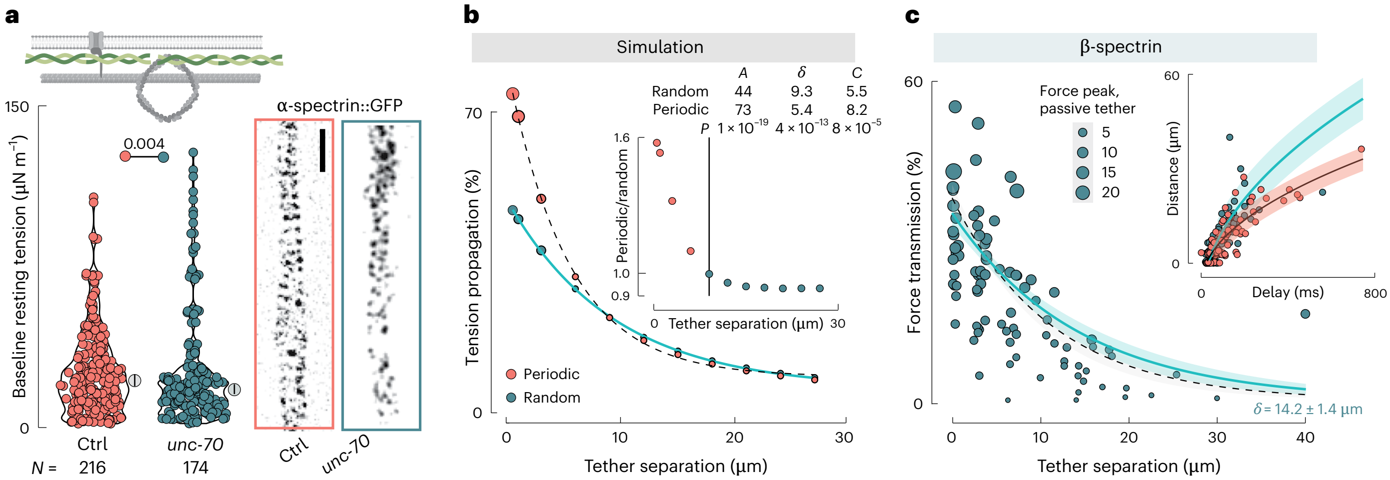

Fig. 5 | Periodicity of the spectrin cytoskeleton supports tension propagation over short distances. a, Influence of the spectrin cytoskeleton on static membrane tension. The median is indicated as a circle, with the vertical bar indicating the confidence interval of 95%. *N*, number of measurements. *P* values above the colour-coded combinations are derived from a two-sided Kolmogoroff–Smirnoff test (Supplementary Table 1). The images on the right show the representative super-resolution images of α-spectrin in wild-type and *unc-70* mutant neurons. Scale bar, 1 µm. **b**, Simulation of tension propagation comparing cells with periodic (red circles) and random (blue circles) obstacle arrangements. Fit parameters of the black, dotted line (periodic) and blue solid line are indicated in the upper right. The inset shows the ratio of propagated tension in the periodic relative to the random case, showing that periodic arrangement favours tension propagation over short distances, whereas random arrangement favours long-distance propagation. The following values for permeabilities have been used: $k_+ = 2.6k$ (instead of $k_+ = 1.5k$) and $k_- = (3k - k_+)/2$). Thus, the value of k_+ increases (0.078 from 0.045 µm^2) and the value of k_- decreases (0.006 from 0.0225 µm^2), with $k = 0.03$ µm^2. **c**, Tension propagation in *unc-70* β-spectrin mutant cells. Inset: tether separation versus pulse delay. The fit is shown as the solid line and the confidence interval, as a shaded band indicate the pulse propagation velocity. The solid lines indicate a fit to an exponential decay (Methods), the error band indicates the 95% confidence interval of the fit and the dotted black line indicates the fit derived from control data (Fig. 1d). The size of the dots corresponds to the absolute force transmitted to the passive tether. Fit parameter *δ* indicates the characteristic length scale.

suggesting that acute actin filament capping (for example, CytoD) and monomer sequestration (for example, LatA) affected membrane permeability differently. However, after the chronic incubation of neurons with 1-µM LatA or 2-µM CytoD overnight, we observed a significant and robust reduction in static membrane tension (LatA, $P = 2 \times 10^{-7}$; CytoD, $P < 1 \times 10^{-16}$; Fig. 4a). The propagation of membrane tension was also differently affected by different drug concentrations. We found that the chronic application of high concentrations of LatA and CytoD resulted in very limited tension propagation (control versus LatA versus CytoD; 11.3 versus 8.1 versus 8.1 µm; Fig. 4b). Overall, this is consistent with our previous observations and other reports, which suggest that neuronal responses to actin disruption are dependent on both drug and concentration, with greater sensitivity to CytoD compared with acute treatments with LatA (refs. 31,65).

We reasoned that different concentrations of latrunculin and cytochalasin perturb different populations of actin filaments, as previously observed in MDCK cells[66]. This could be understood in the transient decoupling of the cortex membrane (increase in *k*) with low concentrations of drugs, followed by a decrease in membrane elasticity (decrease in E_m) in chronic drug application. To understand how propagation is subject to the mechanical properties of the membrane–cytoskeleton composite, we turned to our model and simulated different conditions of E_m and *k*. In fact, a decrease in membrane elasticity leads to a decrease in propagated tension, where an increase in *k* led to increased propagation of tension (Extended Data Fig. 5 and Fig. 4c).

Having established the role of actin in axonal membrane mechanics, we next investigated whether microtubules modulate tension propagation along the membrane. Microtubules are a hallmark of neurons and are known to interact with mechanosensitive ion channels[67,68] and membrane-associated proteins[69], making them strong candidates for influencing membrane tension.

In *C. elegans* TRNs, the microtubule cytoskeleton includes large, crosslinked bundles of specialized 15-protofilament (pf) microtubules, which are highly acetylated[70,71], in addition to the conventional 11-pf type. These bundles are anchored to the plasma membrane via a spectrin/ankyrin-based complex[72].

To test their role, we pulled membrane tethers from TRNs of *mec-12(e1607)* mutants, which lack the acetylated 15-pf microtubules but retain conventional ones[73]. These mutants showed significantly increased baseline membrane tension ($P = 0.002$). One possibility is that disrupting the acetylated bundle activates cortical contractility via Rho signalling, as seen in cultured cells[74]. However, a more likely explanation is that 11-pf microtubules compensate by altering the membrane attachment. Supporting this, treating *mec-12* mutants with nocodazole reversed the elevated membrane tension (Fig. 4d).

Interestingly, *mec-12* mutants also exhibited reduced tension propagation compared with controls (10 versus 12.3 µm), and nocodazole treatment led to an even greater reduction ($P = 0.01$; Fig. 4e,f). These results demonstrate that microtubules support membrane tension propagation in axons and suggest that their loss affects propagation through at least two distinct mechanisms: changes in cytoskeletal rigidity and disruption of membrane anchoring.

Periodicity of actin/spectrin cytoskeleton sets limits on tension propagation

It is well established that dynamic barriers on the cytoplasmic leaflet hinder lateral membrane movement[75]. The actin–spectrin cytoskeleton is important in that it coordinates many transmembrane proteins (ion channels, adhesion receptors, dystroglycans and band 4 proteins) and also binds to the membrane itself[34,76,77], effectively compartmentalizing the membrane[62]. Thus, it is plausible that the periodic spectrin cytoskeleton establishes a barrier that impedes free tension propagation by establishing periodic obstacles. Indeed, when we simulated periodically arranged obstacles, rather than randomly distributed clusters, the overall tension was higher but attenuated over short distances and, therefore, propagated less (Fig. 2f). To better understand how obstacle organization influences tension propagation, we simulated tension dynamics by increasing the value of k_+ to 2.6*k*, which,

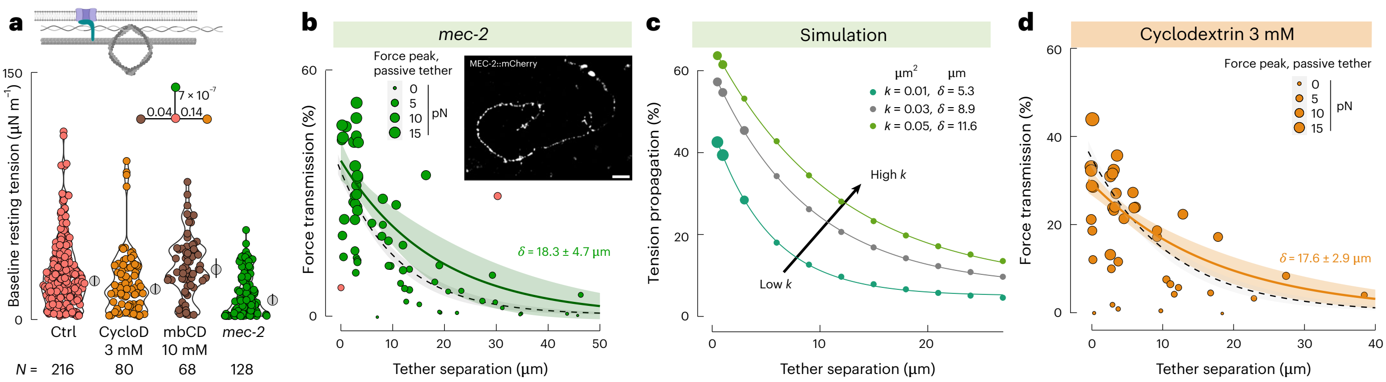

Fig. 6 | Membrane condensation of MEC-2 delimits tension propagation along the membrane. a, Baseline, resting tension during the membrane extrusion from cells mutant for *mec-2* or treated with increasing concentrations of mbCD (3 or 10 mM; Methods). The top schematic highlights channel–cytoskeleton crosslinkers in blue. The median is shown as a circle, with the vertical bar indicating the 95% confidence interval. *N*, number of measurements. The *P* value is derived from a two-sided Kolmogoroff–Smirnoff test. **b**, Force propagation between active and passive tethers for *mec-2* mutant neurons. The solid green line indicates a fit to an exponential decay (Methods), the shaded area indicates the 95% confidence interval of the fit and the dotted black line indicates the fit derived from the control data (Fig. 1d). The size of the dots corresponds to the absolute force transmitted to the passive tether. Inset: fluorescent micrograph of MEC-2:mCherry, distributed along the axon in cultured neurons as a proxy for membrane obstacles. Scale bar, 5 μm. **c**, Simulation of tension propagation comparing cells with decreasing obstacle density and increasing permeability *k*. The simulation corresponds to the periodic case. Hence, the value *k* is used to calculate k_+ and k_-. **d**, Tension propagation for neurons treated with mbCD to sequester cholesterol. The solid orange line indicates a fit to an exponential decay (Methods), the shaded area indicates the 95% confidence interval of the fit and the dotted black line indicates the fit derived from the control data (Fig. 1d). The size of the dots corresponds to the absolute force transmitted to the passive tether.

in turn, decreases the value of $k_- = (3k - k_+)/2$. These changes accentuate the difference between the permeabilities and, hence, represent a more predominant periodic barrier. We compared the outcomes between randomly distributed obstacles and the new setup of periodically arranged ones (Fig. 5b). These simulations revealed that periodic cytoskeletal arrangements enhance tension propagation over short distances. However, at intermediate distances, which depend on specific model parameters such as permeability (k) and membrane elasticity (E_m), random arrangements favoured greater tension spread (Fig. 5b, inset). In other words, the loss of periodicity leads to an increase in tension propagation, especially at large distances.

UNC-70 is the sole β-spectrin homologue in *C. elegans* neurons and forms a complex with α-spectrin, and can bind to both the actin cytoskeleton and the membrane with its pleckstrin homology domain[78]. In *C. elegans*, similar to the neuronal cytoskeleton in mammals, both components form a characteristic periodicity of 190 nm in vitro and in vivo[26,34,57]. This periodicity is more variable in intact animals[79] and completely lost in the absence of functional UNC-70, as visualized using α-spectrin as a proxy for the spectrin network organization (Fig. 5a)[26]. Similar to the model predictions (Fig. 5b), the propagation at short distances in the spectrin mutant is lower than in the wild type, but propagates significantly further into the neurite of *unc-70* null mutants (Fig. 5c; $P = 0.02$), suggesting that the loss of β-spectrin leads to discretely clustered domains of transmembrane proteins[80] and a concomitant increase in permeability.

However, our model does not rule out other factors, such as transmembrane receptor endocytosis, which may further lead to an increase in tension propagation in the spectrin mutant[81]. Together, our results from both experiments and modelling suggest that periodic membrane obstacles as well as components of the cytoskeleton locally restrict and limit the extent of membrane tension propagation. Our observations suggest that the distinct periodicity of the actin/spectrin network is a mediator of the organization of transmembrane and membrane-associated proteins and, thus, the propagation of tension in neurons.

Stomatin MEC-2 condensation at the membrane impedes tension propagation

Last, we tested whether obstacles in the membrane can indeed influence the propagation of membrane tension. We have previously shown that MEC-2 (mec, mechanosensory), a stomatin homologue associated with stiffened membrane domains[40], forms biomolecular condensates proximal to the inner leaflet of the plasma membrane[29]. MEC-2 condensates exhibit a discrete, punctate distribution in both in vivo and in vitro settings, with a typical spacing of 2–4 μm and 1–2 μm (Fig. 6b, inset), respectively. To understand whether the condensation of MEC-2 on the plasma membrane influences tension propagation, we performed tether extrusion in *mec-2* knockout animals. The baseline tension of the resting membrane was lower than that of the control neurites, indicating that the MEC-2 stomatin may also influence tension propagation (Fig. 6a). Interestingly, we also observed substantially larger tension propagation in the neurite of *mec-2* mutants (control versus *mec-2*; 11.3 versus 18.5 μm). Thus, we asked whether obstacles like MEC-2 impede tension propagation in our model. Indeed, as shown above, our simulations predicted that membranes with a higher permeability would enhance tension propagation (Fig. 6c). Therefore, removing MEC-2, which binds to the inner leaflet of the plasma membrane through its cholesterol-binding ability, reduces obstacle density, increases *k* and increases tension propagation.

MEC-2 stomatin is a cholesterol-binding protein, and the disruption of its cholesterol-binding ability alters the regulation of the ion channel[41,82]. The addition of cholesterol to biomembranes has been shown to increase the membrane expansion modulus (E_m), effectively making the membranes stiffer[83]. This prompted us to investigate how cholesterol depletion affects tension propagation in cultured neurons. To this end, we treated cells with methyl-β-cyclodextrin (mbCD) to extract membrane cholesterol and confirmed depletion by monitoring the loss of filipin fluorescence, a dye commonly used to visualize membrane cholesterol (Extended Data Fig. 7a,b). As shown above, stiffer membranes propagate tension better (Extended Data Fig. 4d); consequently, we would expect that the addition of mbCD to remove cholesterol lowers tension propagation. However, experiments revealed the opposite: treating neurons with 3-mM mbCD to sequester cholesterol significantly increased tension propagation (control versus treated: 12 μm versus 17.6 μm), similar to the effects observed with the genetic disruption of *mec-2* (Fig. 6d). This surprising increase in tension propagation is inconsistent with the expected effect of softer membranes alone (Fig. 2g). Instead, we propose that it results from a reduction in obstacle density and clustering within the membrane, as seen in both *mec-2* mutants and cholesterol-depleted neurons. Indeed, a mutant MEC-2 protein with a conversion of proline to serine (P134S) that cannot bind to cholesterol was shown to disrupt the proper localization and organization of MEC-2 in the membrane of TRNs[41]. Collectively, these data suggest that MEC-2 condensates act as an obstacle, interacting with cholesterol in the membrane to limit the propagation of membrane tension.

Conclusion

Using *C. elegans* as a model for mechanotransduction and neuroscience, we dissected the molecular signature of mechanical stress propagation along the neuronal membrane of sensory neurites in neurons responsible for the sense of touch and proprioception. With an optical-tweezers-based membrane tether extrusion assay, we found that, unlike our previous observations of tubes extruded from zebrafish progenitor cells[3,45] or the soma of cultured TRN[31,32], the tension did not remain constant during the extrusion protocol, suggesting a limited membrane reservoir that cannot buffer tension gradients in axons[7]. We found that steep gradients of membrane tension propagate fast (>120 μm s^{-1}) but only to a limited distance (<20 μm). We also observed considerable variability in the propagation length scale (Fig. 1d) and velocity (Extended Data Fig. 3e), which may reflect the involvement of distinct propagation mechanisms, such as transmission through the membrane, the cytoskeleton, the viscoelastic cytoplasm, and the density and arrangements of obstacles in the membrane. It may also suggest that obstacles are not homogeneously distributed along the neurite, with varying densities in the proximal and distal regions, as observed with MEC-2 in our cultures (Extended Data Fig. 7c).

Our experimental results are consistent with predictions from a biophysical model that a higher permeability (lower obstacle density) through membrane–cortex disruption propagates tension farther. Interestingly, we observed a significant dose-dependent effect when altering the actin and microtubule cytoskeleton and spectrin organization. For example, actin depolymerization with varying concentrations of LatA and CytoD had opposing effects on tension propagation. At an acute delivery of low concentrations, the propagation distance increased, presumably due to the transient decoupling of membrane–cortex binders, whereas at high and chronic treatments, tension propagation was reduced. Therefore, we speculate that chronic actin depolymerization disrupted the caveolae and other membrane domains, essentially increasing the available membrane lipid reservoir, as also proposed previously[61,84,85]. Indeed, our collective results show that there is no strong correlation between the extent of membrane tension propagation, velocity and resting tension, indicating that each property is regulated by different mechanisms.

We uncovered that periodic obstacle arrangement supports tension propagation over short distances, whereas more homogeneous and randomly organized obstacles better support long-range tension propagation. We propose that mechanical signals must remain confined to be locally processed, much like local computations at synapses. Why might restricted propagation be advantageous? One possibility is that it enhances the cell's ability to detect precise, localized mechanical cues, enabling the parallel processing of simultaneous stimuli and targeted responses. Allowing unrestricted propagation of mechanical information along the axon might blur receptive field boundaries, introducing disruptive background noise. Our data showing that tension propagation is different in touch receptors and proprioceptors suggest a differential expression of membrane obstacles such as cortex crosslinkers. Recent single-cell gene expression datasets show that DVA expresses ten times more of the four-point-one, ezrin, radixin, moesin (FERM) domain protein-1 than TRNs[86], the major Band 4.1N orthologue of the FERM superfamily in *C. elegans* with roles in coupling various transmembrane receptors, channels and adhesion molecules to actin–spectrin cytoskeleton or stomatin proteins[87]. In fact, we have recently shown that FERM domain protein-1 is directly bound to UNC-70 (ref. 79), but future work is necessary to refine the role of FERM domain protein-1 in this process.

Online content

Any methods, additional references, Nature Portfolio reporting summaries, source data, extended data, supplementary information, acknowledgements, peer review information; details of author contributions and competing interests; and statements of data and code availability are available at https://doi.org/10.1038/s41567-025-03037-x.

References

1. Ghisleni, A. & Gauthier, N. C. Mechanotransduction through membrane tension: it's all about propagation? *Curr. Opin. Cell Biol*. **86**, 102294 (2024).
2. Le Roux, A.-L., Quiroga, X., Walani, N., Arroyo, M. & Roca-Cusachs, P. The plasma membrane as a mechanochemical transducer. *Philos. Trans. R. Soc. B* **374**, 20180221 (2019).
3. Diz-Muñoz, A. et al. Control of directed cell migration in vivo by membrane-to-cortex attachment. *PLoS Biol* **8**, e1000544 (2010).
4. Sukharev, S. & Sachs, F. Molecular force transduction by ion channels: diversity and unifying principles. *J. Cell Sci*. **125**, 3075–3083 (2012).
5. Appadurai, D. et al. Plasma membrane tension regulates eisosome structure and function. *Mol. Biol. Cell* **31**, 287–303 (2020).
6. Dai, J. & Sheetz, M. P. Cell membrane mechanics. *Methods Cell Biol* **55**, 157–171 (1997).
7. Raucher, D. & Sheetz, M. P. Characteristics of a membrane reservoir buffering membrane tension. *Biophys. J*. **77**, 1992–2002 (1999).
8. Datar, A., Bornschlögl, T., Bassereau, P., Prost, J. & Pullarkat, P. A. Dynamics of membrane tethers reveal novel aspects of cytoskeleton-membrane interactions in axons. *Biophys. J*. **108**, 489–497 (2015).
9. Brownell, W. E., Qian, F. & Anvari, B. Cell membrane tethers generate mechanical force in response to electrical stimulation. *Biophys. J*. **99**, 845–852 (2010).
10. Das, R. et al. An asymmetric mechanical code ciphers curvature-dependent proprioceptor activity. *Sci. Adv* **7**, eabg4617 (2021).
11. Pradhan, S., Williams, M. A. K. & Hale, T. K. Changes in the properties of membrane tethers in response to HP1a depletion in MCF7 cells. Biochem. *Biophys. Res. Commun* **587**, 126–130 (2022).
12. Dai, J., Sheetz, M. P., Wan, X. & Morris, C. E. Membrane tension in swelling and shrinking molluscan neurons. *J. Neurosci*. **18**, 6681–6692 (1998).
13. Rangamani, P. The many faces of membrane tension: challenges across systems and scales. *Biochim. Biophys. Acta Biomembr*. **1864**, 183897 (2022).
14. Mashanov, G. I. et al. Heterogeneity of cell membrane structure studied by single molecule tracking. *Faraday Discuss* **232**, 358–374 (2021).
15. Shi, Z., Graber, Z. T., Baumgart, T., Stone, H. A. & Cohen, A. E. *Cell membranes resist flow*. *Cell* **175**, 1769–1779.e13 (2018).
16. Rangamani, P., Mandadap, K. K. & Oster, G. Protein-induced membrane curvature alters local membrane tension. *Biophys. J*. **107**, 751–762 (2014).
17. Belly, H. D. et al. *Cell protrusions and contractions generate long-range membrane tension propagation*. *Cell* **186**, 3049–3061.e15 (2023).
18. Shi, Z., Innes-Gold, S. & Cohen, A. E. Membrane tension propagation couples axon growth and collateral branching. *Sci. Adv*. **8**, eabo1297 (2022).
19. Perez, C. G. et al. Rapid propagation of membrane tension at retinal bipolar neuron presynaptic terminals. *Sci. Adv*. **8**, eabl4411 (2022).

20. Jauffred, L., Callisen, T. H. & Oddershede, L. B. Visco-elastic membrane tethers extracted from escherichia coli by optical tweezers. *Biophys. J.* **93**, 4068–4075 (2007).
21. Guilford, W. H., Tournas, J. A., Dascalu, D. & Watson, D. S. Creating multiple time-shared laser traps with simultaneous displacement detection using digital signal processing hardware. *Anal. Biochem.* **326**, 153–166 (2004).
22. Capitanio, M., Cicchi, R. & Pavone, F. S. Continuous and time-shared multiple optical tweezers for the study of single motor proteins. *Opt. Laser Eng.* **45**, 450–457 (2007).
23. Català-Castro, F. et al. Measuring age-dependent viscoelasticity of organelles, cells and organisms with time-shared optical tweezer microrheology. *Nat. Nanotechnol.* **20**, 411–420 (2025).
24. Sanzeni, A. et al. Somatosensory neurons integrate the geometry of skin deformation and mechanotransduction channels to shape touch sensing. *eLife* **8**, e43226 (2019).
25. Krieg, M., Dunn, A. R. & Goodman, M. B. Mechanical systems biology of *C. elegans* touch sensation. *BioEssays* **37**, 335–344 (2015).
26. Krieg, M. et al. Genetic defects in β-spectrin and tau sensitize *C. elegans* axons to movement-induced damage via torque-tension coupling. *eLife* **6**, e20172 (2017).
27. Das, A. et al. *C. elegans* touch receptor neurons direct mechanosensory complex organization via repurposing conserved basal lamina proteins. *Curr. Biol.* **34**, 3133–3151.e10 (2024).
28. Cueva, J. G., Mulholland, A. & Goodman, M. B. Nanoscale organization of the MEC-4 DEG/ENaC sensory mechanotransduction channel in Caenorhabditis elegans touch receptor neurons. *J. Neurosci.* **27**, 14089–14098 (2007).
29. Sanfeliu-Cerdán, N. et al. A MEC-2/stomatin condensate liquid-to-solid phase transition controls neuronal mechanotransduction during touch sensing. *Nat. Cell Biol.* **25**, 1590–1599 (2023).
30. O'Hagan, R., Chalfie, M. & Goodman, M. B. The MEC-4 DEG/ENaC channel of Caenorhabditis elegans touch receptor neurons transduces mechanical signals. *Nat. Neurosci.* **8**, 43–50 (2005).
31. Krieg, M., Dunn, A. R. & Goodman, M. B. Mechanical control of the sense of touch by β-spectrin. *Nat. Cell Biol.* **16**, 224–233 (2014).
32. Vásquez, V., Krieg, M., Lockhead, D. & Goodman, M. B. Phospholipids that contain polyunsaturated fatty acids enhance neuronal cell mechanics and touch sensation. *Cell Rep* **6**, 70–80 (2014).
33. Bennett, V. & Healy, J. Membrane domains based on ankyrin and spectrin associated with cell-cell interactions. *Cold Spring Harb. Perspect. Biol.* **1**, a003012 (2009).
34. Xu, K., Zhong, G. & Zhuang, X. Actin, spectrin, and associated proteins form a periodic cytoskeletal structure in axons. *Science* **339**, 452–456 (2013).
35. Deng, H. et al. Spectrin couples cell shape, cortical tension, and Hippo signaling in retinal epithelial morphogenesis. *J. Cell Biol.* **219**, e201907018 (2020).
36. Fletcher, G. C. et al. Mechanical strain regulates the Hippo pathway in. *Drosophila*. *Development* **145**, dev159467 (2018).
37. Dubey, S. et al. The axonal actin-spectrin lattice acts as a tension buffering shock absorber. *eLife* **9**, e51772 (2020).
38. Mylvaganam, S. et al. The spectrin cytoskeleton integrates endothelial mechanoresponses. *Nat. Cell Biol.* **24**, 1226–1238 (2022).
39. Lorenzo, D. N. et al. ßII-spectrin promotes mouse brain connectivity through stabilizing axonal plasma membranes and enabling axonal organelle transport. *Proc. Natl Acad. Sci. USA* **116**, 15686–15695 (2019).
40. Qi, Y. et al. Membrane stiffening by STOML3 facilitates mechanosensation in sensory neurons. *Nat. Commun.* **6**, 8512 (2015).
41. Huber, T. B. et al. Podocin and MEC-2 bind cholesterol to regulate the activity of associated ion channels. *Proc. Natl Acad. Sci. USA* **103**, 17079–17086 (2006).
42. Bussell, S. J., Koch, D. L. & Hammer, D. A. Effect of hydrodynamic interactions on the diffusion of integral membrane proteins: diffusion in plasma membranes. *Biophys. J.* **68**, 1836–1849 (1995).
43. Hochmuth, R. M., Shao, J. Y., Dai, J. & Sheetz, M. P. Deformation and flow of membrane into tethers extracted from neuronal growth cones. *Biophys. J.* **70**, 358–369 (1996).
44. Li, Z. et al. Membrane tether formation from outer hair cells with optical tweezers. *Biophys. J.* **82**, 1386–1395 (2002).
45. Krieg, M., Helenius, J., Heisenberg, C.-P. & Müller, D. J. A bond for a lifetime: employing membrane nanotubes from living cells to determine receptor-ligand kinetics. *Angew. Chem. Int. Ed.* **47**, 9775–9777 (2008).
46. Borghi, N. & Brochard-Wyart, F. Tether extrusion from red blood cells: integral proteins unbinding from cytoskeleton. *Biophys. J.* **93**, 1369–1379 (2007).
47. Bar-Ziv, R. & Moses, E. Instability and 'pearling' states produced in tubular membranes by competition of curvature and tension. *Phys. Rev. Lett.* **73**, 1392–1395 (1994).
48. Sheetz, M. P. Cell control by membrane-cytoskeleton adhesion. *Nat. Rev. Mol. Cell Biol.* **2**, 392–396 (2001).
49. Li, W., Feng, Z. & Sternberg, P. W. A *C. elegans* stretch receptor neuron revealed by a mechanosensitive TRP channel homologue. *Nature* **440**, 684–687 (2006).
50. Argudo, D., Capponi, S., Bethel, N. P. & Grabe, M. A multiscale model of mechanotransduction by the ankyrin chains of the NOMPC channel. *J. Gen. Physiol.* **151**, 316–327 (2019).
51. Wang, Y. et al. The push-to-open mechanism of the tethered mechanosensitive ion channel NompC. *eLife* **10**, e58388 (2021).
52. Brohawn, S. G., Su, Z. & MacKinnon, R. Mechanosensitivity is mediated directly by the lipid membrane in TRAAK and TREK1 K^+ channels. *Proc. Natl Acad. Sci. USA* **111**, 3614–3619 (2014).
53. Krieg, M., Pidde, A. & Das, R. Mechanosensitive body–brain interactions in *Caenorhabditis elegans*. *Curr. Opin. Neurobiol.* **75**, 102574 (2022).
54. Katta, S., Krieg, M. & Goodman, M. B. Feeling force: physical and physiological principles enabling sensory mechanotransduction. *Annu. Rev. Cell Dev. Biol.* **31**, 347–371 (2015).
55. Eastwood, A. L. et al. Tissue mechanics govern the rapidly adapting and symmetrical response to touch. *Proc. Natl Acad. Sci. USA* **112**, E6955–E6963 (2015).
56. Nekimken, A. L. et al. Pneumatic stimulation of *C. elegans* mechanoreceptor neurons in a microfluidic trap. *Lab Chip* **17**, 1116–1127 (2017).
57. D'Este, E., Kamin, D., Göttfert, F., El-Hady, A. & Hell, S. W. STED nanoscopy reveals the ubiquity of subcortical cytoskeleton periodicity in living neurons. *Cell Rep* **10**, 1246–1251 (2015).
58. Coste, B. et al. Piezo1 and Piezo2 are essential components of distinct mechanically activated cation channels. *Science* **330**, 55–60 (2010).
59. Kahn-Kirby, A. H. et al. Specific polyunsaturated fatty acids drive TRPV-dependent sensory signaling in vivo. *Cell* **119**, 889–900 (2004).
60. Else, P. L. The highly unnatural fatty acid profile of cells in culture. *Prog. Lipid Res.* **77**, 101017 (2020).
61. Dharan, R. et al. Intracellular pressure controls the propagation of tension in crumpled cell membranes. *Nat. Commun.* **16**, 91 (2025).
62. Rentsch, J. et al. Sub-membrane actin rings compartmentalize the plasma membrane. *J. Cell Biol.* **223**, e202310138 (2024).
63. Spector, I., Shochet, N., Kashman, Y. & Groweiss, A. Latrunculins: novel marine toxins that disrupt microfilament organization in cultured cells. *Science* **219**, 493–495 (1983).

64. Schliwa, M. et al. Action of cytochalasin D on cytoskeletal networks. *J. Cell Biol.* **92**, 79–91 (1982).
65. Qu, Y., Hahn, I., Webb, S. E., Pearce, S. P. & Prokop, A. Periodic actin structures in neuronal axons are required to maintain microtubules. *Mol. Biol. Cell* **28**, 296–308 (2017).
66. Stevenson, B. R. & Begg, D. A. Concentration-dependent effects of cytochalasin D on tight junctions and actin filaments in MDCK epithelial cells. *J. Cell Sci.* **107**, 367–375 (1994).
67. Liang, X., Madrid, J. & Howard, J. The microtubule-based cytoskeleton is a component of a mechanical signaling pathway in fly campaniform receptors. *Biophys. J.* **107**, 2767–2774 (2014).
68. Burke, S. D. et al. Solving baroreceptor mystery: role of PIEZO ion channels. *J. Am. Soc. Nephrol.* **30**, 911–913 (2019).
69. Morley, S. J. et al. Acetylated tubulin is essential for touch sensation in mice. *eLife* **5**, e20813 (2016).
70. Chalfie, M. & Thomson, J. N. Structural and functional diversity in the neuronal microtubules of *Caenorhabditis elegans*. *J. Cell Biol.* **93**, 15–23 (1982).
71. Lockhead, D. et al. The tubulin repertoire of *C. elegans* sensory neurons and its context-dependent role in process outgrowth. *Mol. Biol. Cell* **27**, 3717–3728 (2016).
72. He, L. et al. Cortical anchoring of the microtubule cytoskeleton is essential for neuron polarity. *eLife* **9**, e55111 (2020).
73. Chalfie, M. & Au, M. Genetic control of differentiation of the *Caenorhabditis elegans* touch receptor neurons. *Science* **243**, 1027–1033 (1989).
74. Liu, D. P., Chrzanowska-Wodnicka, M. & Burridge, K. Microtubule depolymerization induces stress fibers, focal adhesions, and DNA synthesis via the GTP-binding protein Rho. *Cell Adhes. Commun.* **5**, 249–255 (1998).
75. Edidin, M., Kuo, S. C. & Sheetz, M. P. Lateral movements of membrane glycoproteins restricted by dynamic cytoplasmic barriers. *Science* **254**, 1379–1382 (1991).
76. Bennett, J. S. et al. Spatially-resolved rotational microrheology with an optically-trapped sphere. *Sci. Rep.* **3**, 1759 (2013).
77. Garrido, J. J. et al. A targeting motif involved in sodium channel clustering at the axonal initial segment. *Science* **300**, 2091–2094 (2003).
78. Baines, A. J. Evolution of spectrin function in cytoskeletal and membrane networks. *Biochem. Soc. Trans.* **37**, 796–799 (2009).
79. Malaiwong, N. et al. Mechanical load conditions the spectrin network to 'runon' proteolysis and promotes early onset neurodegeneration. Preprint at *bioRxiv* https://doi.org/10.1101/2024.11.04.621798 (2024).
80. Ghisleni, A., Bonilla-Quintana, M., Crestani, M., Rangamani, P. & Gauthier, N. C. Mechanically induced conformational transition of spectrin in the mammalian cell cortex. *Biophys. J.* **122**, 263A (2024).
81. Wernert, F. et al. The actin-spectrin submembrane scaffold restricts endocytosis along proximal axons. *Science* **385**, eado2032 (2024).
82. Brown, A. L., Liao, Z. & Goodman, M. B. Mec-2 and Mec-6 in the Caenorhabditis elegans sensory mechanotransduction complex: auxiliary subunits that enable channel activity. *J. Gen. Physiol.* **131**, 605–616 (2008).
83. Needham, D. & Nunn, R. S. Elastic deformation and failure of lipid bilayer membranes containing cholesterol. *Biophys. J.* **58**, 997–1009 (1990).
84. Hochmuth, R. M. Micropipette aspiration of living cells. *J. Biomech.* **33**, 15–22 (2000).
85. Echarri, A. & Pozo, M. A. D. Caveolae—mechanosensitive membrane invaginations linked to actin filaments. *J. Cell Sci.* **128**, 2747–2758 (2015).
86. Taylor, S. R. et al. Molecular topography of an entire nervous system. *Cell* **184**, 4329–4347.e23 (2021).
87. Yang, Q., Liu, J. & Wang, Z. 4.1N-mediated interactions and functions in nerve system and cancer. *Front. Mol. Biosci.* **8**, 711302 (2021).

Methods

C. elegans strains and maintenance

Strains were maintained and manipulated under standard conditions[88]. All strains used in this study are enumerated in Supplementary Table 2. Nematode strains were grown at 20 °C on nematode growth medium plates with OP50 bacteria and synchronized using the standard alkaline hypochlorite treatment method[89].

Primary cell culture and membrane extrusion

TRN primary cell culture. Primary cell culture was performed as described in refs. 10,31. In short, gravid hermaphrodites grown onto large, peptone-enriched plates seeded with *E. coli* NA22 bacteria at 20–25 °C were collected with MilliQ water and bleached following regular procedures[89]. Eggs were washed three times with egg buffer (118-mM NaCl, 48-mM KCl, 2-mM $CaCl_2$, 2-mM $MgCl_2$ and 25-mM HEPES at pH 7.3 and 340 mOsm) and separated through a final sucrose density gradient of 30% generated by 20-min centrifugation at 1,300*g*. Once the eggs were collected in a new vial, they were washed twice with the egg buffer and treated with chitinase (0.5 U ml^{-1}) for 40 min to digest their egg shell. The reaction was stopped with the L15 medium. The embryos were then dissociated by passing the solution ten times through a 25-G needle and filtered with a 5-μm Durapore filter (Millipore). Finally, cells were pelleted by 3-min centrifugation at 400*g* and resuspended with L15 medium. Cells were seeded at a density of 1.5×10^6 ml^{-1} in optical trapping chambers (see below) and 1 ml of L15 medium was added after 3 h. They were cultured at 25 °C and fresh medium was changed (1–2 ml) every day. All the experiments were performed between 2 and 4 days after isolation. CO_2-independent L15 tissue culture medium supplemented with heat-inactivated bovine calf serum (10% v/v; FBS 11A Capricorn Scientific), penicillin (10 mg ml^{-1}) and streptomycin (100 units; L0022 Biowest) was used throughout the study[31].

The drugs were added 24–48 h after isolation. Nocodazole (M1404, Sigma) was added at a final concentration of 1 μg ml^{-1}. CytoD (10-mM stock in dimethyl sulfoxide; C2618, Sigma) was diluted 1:5,000 in L15 medium to a 2-μM final concentration. LatA (10-mM stock, L5163, Sigma) was diluted in L15 medium to a final concentration of 500 nM, 1 μM or 10 μM. methyl-beta-cyclodextrin (mbCD; C4555, Sigma) was added to the final concentration of 3 or 10 mM. Cells were incubated with nocodazole, mbCD or LatA (acute) for 30 min, whereas treatments with CytoD and LatA were incubated overnight at 25 °C, followed by three washes of L15 with the corresponding drug. Hypo-osmotic shocks were perfomed by diluting 1:1 L15 medium in water.

Cholesterol staining with filipin

Cells were treated with 10-mM mbCD 48 h post-isolation, as described above. After a 30-min incubation, both treated and untreated (control) cells were washed three times with phosphate-buffered saline (PBS). Cells were then fixed with 4% paraformaldehyde (in PBS) for 15 min at room temperature, followed by three additional PBS washes. Filipin III (Fermentek, FLP-001) was added at a final concentration of 0.05 mg ml^{-1} in PBS, prepared from a 5 mg ml^{-1} stock solution in dimethyl sulfoxide, as described[90]. After a 2-h incubation in the dark (note that filipin is highly photosensitive), the samples were washed three times with PBS. Imaging was performed on a TCS SP8 microscope (Leica Microsystems), equipped with an HC PL APO CS2 ×60/1.4 oil-immersion objective and a hybrid detector. Images were acquired at a 16-bit depth. Filipin III was excited at 405 nm (65.3 μW at the sample plane; 40% transmittance) and fluorescence emission was collected in the 410–465-nm range. For the analysis of the filipin fluorescence intensity, cells were segmented using the trainable Weka segmentation plugin in ImageJ/Fiji (ImageJ 1.53f51). This machine-learning-based tool was trained to distinguish cell regions from the background using manually annotated training data. The resulting segmentation masks were applied to identify individual cells as regions of interest. The total fluorescence intensity within each region of interest was measured, and the background signal was subtracted by quantifying fluorescence in cell-free regions. Statistics were derived from a two-tailed unpaired Student's *t*-test.

Optical micromanipulation and confocal microscopy

A multimodal platform was used that combined spinning-disc confocal microscopy and optical micromanipulation. Briefly, an optical micromanipulation unit (SENSOCELL, IMPETUX) modulated with a pair of acousto-optic deflectors was coupled to the rear epifluorescence port of an inverted research microscope (Nikon Ti2 Eclipse). The optical traps were created at the focal plane of a ×60/1.2 water-immersion microscope objective (Nikon). A spinning-disc confocal unit (Dragonfly, Andor) was coupled to the left port of the microscope. A detailed description of the setup is provided elsewhere[91].

Optical trapping chambers containing primary culture cells were built in a #1.5H glass-bottom plate (GWST-5040, WillCo). Dishes were coated with a 50-μm polydimethylsiloxane layer, from which a 1×1 cm^2 cavity was drawn, in which the cells were seeded as that done in ref. 10. Before the experiment, cells were gently rinsed with L15 medium three times and the cavity was filled with 50 μl of a solution containing 1-μm-diameter polystyrene beads (red fluorescent, carboxylate modified: F8816, Thermo Fisher, 1:2,000 dilution). Finally, the cavity was cautiously closed with a 25×25-mm^2 coverslip and mounted on the microscope.

All optical force measurements in this study were carried out through calibration-free detection of light momentum changes using a direct force sensor (SENSOCELL, IMPETUX), collecting the light emerging from the optical traps. The nominal trap stiffness was 3 pN μm^{-1} mW^{-1} (for polystyrene, $2R = 1$ μm bead). For a typical experiment with a 360-mW trap (5 W of output laser power at 1,064 nm), a trapping stiffness of 1,080 pN μm^{-1} results into a roll-off frequency of $f_c = k/(2\pi\gamma) \approx 17.7$ kHz (ref. 92), where $\gamma = 6\pi\,\eta(T)Rb$ is the friction coefficient ($\eta(T)$, medium viscosity; D, bead diameter; b, Faxén hydrodynamic correction for $z = 2$ μm with respect to the coverglass; Supplementary Information and ref. 93). Room temperature around the microscope table was $T_{room} = 21$ °C, whereas the local temperature around the optically trapped beads was estimated to be to be $T = 24.6$ °C (ref. 94).

Simultaneous optical trapping of several microbeads was performed by time sharing the laser spot at 25 kHz. Details of time sharing can be found in ref. 23. In short, the 1,064-nm laser beam with power P is split into two alternating traps every 40 μs using a pair of acousto-optic defelectors. During the 40-μs trapping period, each bead feels the power P, and thus, the power with which the bead is trapped remains constant and does not change with the number of traps. Consequently, the stiffness of the trap remains constant and is independent of the number of traps. A thorough analysis of the dual-trap time-sharing measurement protocol is introduced in the Supplementary Information.

Because the refreshing rate of the two traps exceeds the timescale over which the bead can diffuse away or be retracted into the cell, this allows for a quasi-simultaneous measurement of membrane tension at different sites of the neuronal axon through the extrusion of membrane nanotubes (Supplementary Information). Because *C. elegans* is a poikilotherm organism and thrives between 15 and 25 °C, optical trapping was performed at room temperature (20 °C) and the dynamic viscosity of L15 supplemented with 10% fetal bovine serum was 0.930 ± 0.034 mPa s, as determined before[95]. Dynamic control of the optical traps was performed with the manufacturer software (LightACE 1.6.2, IMPETUX) and automated with a software development kit in LabVIEW (2020 version, National Instruments).

Extrusion of membrane nanotubes and spatiotemporal force spectroscopy. Once both microspheres were optically trapped, brief contact (~1 s) with the axonal membrane was sufficient to extrude two lipid nanotubes (Fig. 1a). Maintaining these tethers in a fixed position required a holding force F_{rest}, which reflects the baseline (resting) membrane tension. Although trap 2 was held constant, the active trap 1 was moved at 40 µm s^{-1} for 10 µm. The extrusion of a nanotube translated into an increase in the force signal, which reached a peak, F_{peak}, of increasing height for a higher pulling velocity. Once the extruding bead stopped, the peak force was followed by viscoelastic relaxation, reaching a static tension value, F_{static} (Fig. 1b). The tether neck from which the membrane nanotube was extruded could slide along the axon as the optically trapped bead was moved parallel to it (Supplementary Video 1), reaching a perpendicular orientation with respect to the axon to minimize the nanotube length[8]. This allowed us to separate the tether necks apart (distance d, Fig. 1c) to measure membrane tension diffusion at increasing distances along the axon.

The friction of the microbead with respect to water was calculated using the Stokes drag expression corrected for the bead–surface interaction[93]:

$$F_{\text{drag}} = \frac{6\pi\,\eta(T)\,R}{1 - \frac{9R}{16h} - \frac{R^3}{8h^3}}\,v, \qquad (3)$$

where v is the trap velocity, h is the bead–surface separation, R is the bead radius and $\eta(T)$ is the temperature-dependent viscosity of the medium. The denominator in equation (3) accounts for the bead–surface hydrodynamic coupling[93]. Heating does not have an affect on neuron viability and signalling because neurons are grown in glass, which has high thermal conductivity[94]. The approach and retraction cycles of a trapped microsphere without attachment to the neuronal membrane did not elicit cellular changes[10].

Calculating resting membrane tension. The baseline resting tension of the membrane was determined on the passive and active tethers before each tension propagation experiment (Fig. 1c and Extended Data Fig. 3b). We divided the measured force with the predetermined correction factor h to account for the time-sharing deviation (Supplementary Information). As shown in Extended Data Fig. 2c, when these values come from dual-tether extrusion experiments, the correction factor was determined to be 0.63. The resting tension extracted from the active and passive tethers were not statistically different (Extended Data Fig. 3a); consequently, we pooled these values to obtain the population measure of σ_{rest}. This value depended not only on the cell type but also on the pharmacological treatment, and provides information on the mechanical coupling of the membrane to the cortex and surface tension in the plane[3]. We calculated the effective membrane tension as before[48] using the well-known relation, assuming a bending rigidity of 2.7×10^{-19} N m (ref. 43):

$$\sigma_{\text{rest}} = \frac{F_{\text{rest}}^2/h}{8\pi^2\kappa}. \qquad (4)$$

Peak and decay membrane tension dynamics. Membrane tension during tether pull and time relaxation was fitted to an exponential + linear load function (equation (5a)) and a stretched exponential decay (equation (5b)), respectively, to both active and passive tethers as follows (Extended Data Fig. 8 (insets)). A stretched exponential decay captures the multiple timescales arising from molecular heterogeneity[96,97].

$$f_1(t) = A_1 t - B_1 \mathrm{e}^{-t/\tau_1} + C_1 \qquad (5a)$$

$$f_2(t) = A_2 + (B_2 - A_2)\mathrm{e}^{-(t/\tau_2)^{q_2}} \qquad (5b)$$

From the fits, we obtained the force peaks for the active and passive tethers as $F_{\text{peak}}^{\text{act}} = f_1^{\text{act}}(t = t_1)$ and $F_{\text{peak}}^{\text{pass}} = f_1^{\text{pass}}(t = t_1)$, as well as the static tension values after the relaxation, namely, $F_{\text{static}}^{\text{act}} = f_2^{\text{act}}(t = t_2)$ and $F_{\text{static}}^{\text{pass}} = f_2^{\text{pass}}(t = t_2)$. Extended Data Fig. 8 provides a graphical explanation.

Measuring force propagation between two tethers along the plasma membrane. The experiments involved an active trap holding a microsphere, which pulled on the corresponding nanotube at a rate of 40 µm s^{-1}, whereas the passive trap remained stationary. The bead was then approached back to the axon after 5 s. The membrane tension gradients originating from the active bead trap were partially diffused into the passive one (Fig. 1c). As the tether force at zero velocity reads as $F_{\text{rest}} = 2\pi\sqrt{(2\kappa \times \sigma_{\text{rest}})}$, we assume that the change in membrane surface tension at the two tether necks follows equation (1)[10,43], from which the relative change in force on the passive trap, with respect to the active, was calculated as follows:

$$\Delta_{\%}F_{\text{peak}} = \frac{F_{\text{peak}}^{\text{pass}} - F_{\text{rest}}^{\text{pass}}}{F_{\text{peak}}^{\text{act}} - F_{\text{rest}}^{\text{act}}} \times 100, \qquad (6a)$$

$$\Delta_{\%}F_{\text{static}} = \frac{F_{\text{static}}^{\text{pass}} - F_{\text{rest}}^{\text{pass}}}{F_{\text{static}}^{\text{act}} - F_{\text{rest}}^{\text{act}}} \times 100. \qquad (6b)$$

The force transmission (Fig. 1d) reached 40%–50% for the shortest double-tether separation, $d \to 0$. To achieve this, the two beads faced each other and pulled the lipid nanotubes towards opposite directions. For increasing d, the tension rapidly dropped from the active to the passive tether, suggesting effective buffering of the membrane tension along the axon. When 20 µm apart, the tension in the passive nanotube almost vanished ($\Delta F_{\%} < 20\%$).

To determine the best-fitting model and account for both fit quality and model complexity, we employed the AIC for model comparison. The AIC is defined $\mathrm{AIC} = 2k - 2\ln[L]$, where k is the number of estimated parameters and L is the maximum likelihood of the model. Lower AIC values indicate models that achieve a better trade-off between explanatory power and parsimony. All model fitting and AIC calculations were performed in R using the lm() and AIC() functions. We formally compared three functions: $f(x) = A\exp(-x/\delta)$, $g(x) = A\exp(-x/\delta) + C$ and $h(x) = A\exp(-x^2/\delta)$.

To quantify the spatial decay of force propagation, we plotted the ratio of the peak force in the passive tether to the peak force in the active tether as a function of the distance between the two tethers (Fig. 1d) and fitted a monoexponential decay model $\exp(x) = A\exp(-x/\delta)$ using weighted least squares.

Model fitting was performed using the Levenberg–Marquardt algorithm via the nlsLM() function from the minpack.lm library in R. To improve robustness against outliers and heteroscedasticity, we implemented a two-step fitting procedure: an initial fit was used to calculate the residuals, which were then transformed into observation-level weights using a Huber-type loss function (tuning constant, 1.345; ref. 98). These weights were then used in a second fit, which was more robust against influential data points. To identify and visualize influential observations, we computed Cook's distance based on a linearized approximation of the nonlinear model. This was done by fitting a linear model to the same response and predictor variables and calculating the standard leverage-based influence measure using the formula $D_i = \frac{r_i^2}{p \times MSE} \times \frac{h_{ii}}{(1-h_{ii})^2}$, where r_i is the residual for observation i, h_{ii} is the leverage, p is the number of parameters and MSE is the mean squared error of the linear fit. Points with $D_i > 4n$ were flagged as potentially influential and highlighted in the final visualization.

The variance–covariance matrix of parameter estimates was extracted from the fitted model, and 95% confidence intervals on the fitted curves were computed by propagating uncertainty via the Jacobian matrix of the model at the prediction points. In particular, nlsLM yielded narrower 95% confidence intervals compared with nls (which uses the Gauss–Newton algorithm), probably due to improved numerical stability and better conditioning of the Jacobian used in estimating parameter uncertainty. The final plot displays the robust fits and confidence ribbons for both control and test groups across the measured spatial domain.

To account for measurement uncertainties in offset compensation during the optical trap initial momentum calibration procedure[91], the initial fit was weighted using the absolute peak force of the passive tether.

Measuring tension propagation speed from the active to passive tether. The time delay between the two peaks was measured by identifying a maximum in the correlation between the active and passive tether forces, which can be expressed as

$$C = f_{\mathrm{p}} \otimes f_{\mathrm{a}}, \tag{7}$$

where ⊗ represents the correlation operation and was carried out using the xcorr function in MATLAB (v. R2019b). We estimated the mean propagation velocity in each condition by fitting a linear regression of distance (d) on delay (Δt), $d = v\Delta t + b$, so that the slope v is directly equal to the velocity. Because a power-law model with an exponent of 0.5 yielded a lower AIC (593) than the linear model (604), we applied a square transformation to linearize the relationship. To test for statistically significant differences in velocity between treatments, we then modelled the squared distance as a function of delay, $d^2 = \beta_0 + \beta_1\Delta t$, and compared the β_1 coefficients (with their confidence intervals) across treatment groups, as described below.

Tension propagation model

Following ref. 15, we augment the Stokes equation with a drag term $\frac{\eta}{k}\mathbf{v}$, which gives

$$\nabla\sigma = -\eta\nabla^2\mathbf{v} + \frac{\eta}{k}\mathbf{v}, \tag{8}$$

where σ is the tension, $\mathbf{v}$ is the velocity field of the lipid flow, η is the two-dimensional membrane viscosity and k is the Darcy permeability of the array of the obstacles. We also assume the conservation of mass, given by

$$\frac{\partial\rho}{\partial t} + \nabla\cdot(\rho\mathbf{v}) = 0, \tag{9}$$

where ρ is the two-dimensional density of lipids. As in ref. 15, we assume a small perturbation in the lipid density $\rho_0 + \epsilon\rho$; then, $\nabla\cdot((\rho_0+\epsilon\rho)\mathbf{v}) = \nabla(\rho_0+\epsilon\rho)\cdot \mathrm{v} + (\rho_0+\epsilon\rho)\nabla\cdot\mathbf{v} = \rho_0\nabla\cdot\mathbf{v} + \nabla\cdot(\epsilon\rho\mathbf{v})$. Thus, a change in density $\delta\rho$ is given by $-\rho_0\nabla\cdot\mathbf{v}$. Following ref. 15, we assume a linear stress–strain relationship for the membrane tension $\delta\sigma = -E_{\mathrm{m}}\delta\rho/\rho_0$, where E_{m} represents the effective area expansion modulus of the cell membrane. Substituting the change in density, we get $\delta\sigma = E_{\mathrm{m}}\nabla\cdot\mathbf{v}$.

Now, taking the divergence of equation (8) as

$$\nabla\cdot\nabla\sigma = \nabla\cdot\left(\left(-\eta\nabla^2 + \frac{\eta}{k}\right)\mathbf{v}\right) = \eta\left(-\nabla^2 + \frac{1}{k}\right)\nabla\cdot\mathbf{v}, \tag{10}$$

and the above stress–strain relationship gives

$$\frac{E_m}{\eta}\nabla^2\sigma = \left(-\nabla^2 + \frac{1}{k}\right)\frac{\partial\sigma}{\partial t}. \tag{11}$$

Note that, different from ref. 15, we do not assume that the spacing between the transmembrane obstacles is small compared with externally imposed variations in the flow field. This allows us to investigate different spatial configurations of the obstacles.

We solve equation (11) in COMSOL Multiphysics (v. 6.1) using the parameters listed in Supplementary Table 3. The pulling events were simulated by combining the definition of tension in the tether (σ_{t}):

$$\sigma_t = \frac{\kappa}{2r_t^2}, \tag{12}$$

with the area of the tether

$$A = 2\pi r_t l, \tag{13}$$

which gives

$$\sigma_t = \frac{2\kappa\pi^2 l^2}{A^2}. \tag{14}$$

Here κ is the bending stiffness of the membrane, r_{t} is the tether radius and l is its length. Thus, the change in tension due to the pulling of the tether is given by

$$\frac{\mathrm{d}\sigma}{\mathrm{d}t} = \frac{4\kappa\pi^2 l}{A^2}\left(\frac{\mathrm{d}l}{\mathrm{d}t} - \frac{l}{A}\frac{\mathrm{d}A}{\mathrm{d}t}\right). \tag{15}$$

We take $\frac{\mathrm{d}l}{\mathrm{d}t} = \upsilon_{pull}$ and $\frac{\mathrm{d}A}{\mathrm{d}t} = \int_T k\nabla\sigma/\eta$, where T is the perimeter of the tether boundary and υ_{pull} the pulling velocity. The tension propagation curves in Fig. 2 were obtained by measuring the tension at the tip of the active and passive tethers. Note that we assume an initial length of the tether as l_0 and we do not change the geometry of the model during the simulation. Instead, we include the tension flow at the tip of the tether corresponding to equation (15).

Statistics and reproducibility

All the statistical calculations were performed in R (v. 4.2.2, 2022-10-31), Python (v. 3) or MATLAB. The Cliff's delta was chosen as a non-parametric effect size measure to quantify the degree of overlap between two distributions when the data were not normally distributed or when comparing medians instead of means (Supplementary Table 1). Setting X and Y as the two groups, we use $\delta = \frac{\text{Number of times } x>y - \text{Number of times } x<y}{n_x n_y}$, where n_x and n_y are the sample sizes of groups X and Y, respectively. The result is between −1 and 1, where 1 means all values in group $X >$ group Y, −1 means all values in group $X <$ group Y and 0 means complete overlap (no effect).

For standard hypothesis testing, we exclusively performed two-sided tests, unless otherwise indicated in the figure legend. The level of significance for all comparisons was chosen at $\alpha = 0.05$, unless otherwise indicated in the figure or figure legend. No statistical methods were used to predetermine the sample sizes, but our sample sizes are similar to those reported in previous publications. Sample sizes are indicated in the figures. Data collection and analysis were not performed blind to the conditions of the experiments, except when indicated otherwise. Unless otherwise stated, all data have been assumed to not follow a normal distribution. Accordingly, distributions of the baseline resting tensions (σ_{rest}, for example, Fig. 1d) were tested using a Kolmogoroff–Smirnoff test for pairwise comparison using wild-type as a control group. The 95% confidence interval was derived by bootstrapping, in which we randomly sample N data points with replacements from the measured distribution, where N is the sample size of the experimental dataset. This procedure was repeated 1,000 times and the median was calculated each time. Finally, we sort the bootstrapped distribution of medians and select the 2.5th and 97.5th percentiles for the 95% confidence interval.

Only mono- or bipolar, healthy looking neurons were used for the experiment, and cells not clearly showing a differentiated axon/neurite or with extensive neurite branches were not used for measurements. As some treatments have previously been shown to result in aberrant neurite morphologies and branches, this may introduce a bias towards wild-type-like neurons, but avoids confounding effects due to geometry (large-diameter varicosities, branches) and cell–substrate contacts. Tether extrusions with more than one attachment between the axon and bead were excluded from the analysis.

To assess differences in force transmission between the experimental and control conditions, we analysed the ratio of transmitted to active force as a function of distance. The ratio was first log-transformed to normalize the distribution and stabilize variance. A linear regression was then performed with distance as the independent variable and the log-transformed force ratio as the dependent variable.

To account for variability in measurement confidence, the regression was weighted by the absolute value of the transmitted force. This approach reflects the assumption that lower transmitted forces are associated with increased uncertainty and, therefore, should contribute less to the regression model. Comparisons between experimental and control conditions were made by evaluating the difference in regression slopes, testing whether the spatial distribution of force transmission varied significantly across groups. The resulting *P* value quantified the statistical significance of this difference. All analyses were carried out in R, using weighted linear models between x (distance) and y (the force ratio):

$$y = \beta_0 + \beta_1 x + \beta_2 G + \beta_3 x G + \varepsilon,$$

where G is a binary indicator variable for group (0, control; 1, test), ε is the residual error, β_0 is the intercept for the control group, β_1 is the slope for the control group, β_2 represents the difference in intercept between groups and β_3 represents the difference in slope between groups. A statistically significant interaction term (β_3, $P < 0.05$) indicates that the slopes of the regression lines differ significantly between groups. Model fitting was performed in R using the lm() function and statistical tests were based on a t-test: $t = \frac{b_1 - b_2}{\sqrt{S^2_{b_1} + S^2_{b2}}}$, $df = n_1 + n_2 - 4$.

Simulations. Similar to the experiments, we calculated the extent of tension propagation after plotting the ratio of the peak tension in the passive tether to the peak tension in the active tether as a function of the distance between the two tethers (Fig. 2c and Extended Data Fig. 4) and fitted an exponential decay function $\exp(x) = A\exp(-\delta x)$ using weighted least squares. We used the MATLAB function fit.m, and to evaluate the fit, we obtained the root mean squared error. We noticed a systematic underestimation of the exponential fit function for large distances between tethers in the simulations. Although force transmission dissipates for long distances in experiments, we found a residual tension for our given set of parameters in the model simulations, which cannot be captured by the exponential fit. The parameter choices for the model were based on (1) having a physiologically feasible set of parameters and (2) replicating the levels of tension propagation at small distances. Thus, instead of fitting the parameters to the experimental data, we decided to keep the physiologically feasible parameters in the model and attributed the residual tension at long distances to effects that are not accounted for in the model, such as sources and sinks of lipids via endo- and exocytosis. We acknowledge that future iterations of the model should address this discrepancy. To better model the extent of tension propagation, we incoporated an offset C to the exponential function: $\exp(x) = A\exp(-\delta x) + C$. This addition resulted in better fittings, for $k = 0.03\ \mu\text{m}^2$, the AIC decreased from 42.99 to 8.24 in the random case and from 48.95 to 11.06 in the periodic case (the fittings with the offset are shown in Fig. 2). Hence, the exponential decay allowed us to better compare different conditions in the simulations. To test if the difference between conditions of the extent of tension propagation δ was significant, we obtained the confidence interval with the confint.m function and obtained the standard error (SE) with Student's t-inverse cumulative distribution function, tinv.m. Then, we calculated the t-score for a two-tailed t-test by taking $(\delta_{\text{condition1}} - \delta_{\text{condition2}})/\sqrt{\text{SE}^2_{\text{condition1}} + \text{SE}^2_{\text{condition2}}}$.

Reporting summary

Further information on research design is available in the Nature Portfolio Reporting Summary linked to this article.

Data availability

All raw data are available via Zenodo at https://doi.org/10.5281/zenodo.15465212 (ref. 99). Source data are provided with this paper.

Code availability

The code for tension propagation measurements is avaliable via GitHub at https://github.com/RangamaniLabUCSD/Tension-Propagation. The code to perform the time-sharing optical trapping simulations is available via GitLab at https://gitlab.icfo.net/rheo/Tweezers/dualtethersimu.

References

88. Stiernagle, T. Maintenance of *C. elegans*. *WormBook: The Online Review of C. elegans Biology* https://doi.org/10.1895/wormbook.1.101.1 (2006).
89. Porta-de-la-Riva, M., Fontrodona, L., Villanueva, A. & Cerón, J. Basic *Caenorhabditis elegans* methods: synchronization and observation. *J. Vis. Exp.* **64**, e4019 (2012).
90. Biswas, A., Kashyap, P., Datta, S., Sengupta, T. & Sinha, B. Cholesterol depletion by mβcd enhances cell membrane tension and its variations-reducing integrity. *Biophys. J.* **116**, 1456–1468 (2019).
91. Català-Castro, F., Venturini, V., Ortiz-Vásquez, S., Ruprecht, V. & Krieg, M. Direct force measurements of subcellular mechanics in confinement using optical tweezers. *J. Vis. Exp.* **174**, e62865 (2021).
92. Berg-Sørensen, K. & Flyvbjerg, H. Power spectrum analysis for optical tweezers. *Rev. Sci. Instrum.* **75**, 594–612 (2004).
93. Schäffer, E., Nørrelykke, S. F. & Howard, J. Surface forces and drag coefficients of microspheres near a plane surface measured with optical tweezers. *Langmuir* **23**, 3654–3665 (2007).
94. Català, F., Marsà, F., Montes-Usategui, M., Farré, A. & Martín-Badosa, E. Influence of experimental parameters on the laser heating of an optical trap. *Sci. Rep.* **7**, 16052 (2017).
95. Poon, C. Measuring the density and viscosity of culture media for optimized computational fluid dynamics analysis of in vitro devices. *J. Mech. Behav. Biomed. Mater.* **126**, 105024 (2022).
96. Lukichev, A. Physical meaning of the stretched exponential Kohlrausch function. *Phys. Lett. A* **383**, 2983–2987 (2019).
97. Bonfanti, A., Kaplan, J. L., Charras, G. & Kabla, A. Fractional viscoelastic models for power-law materials. *Soft Matter* **16**, 6002–6020 (2020).
98. Huber, P. Robust estimation of a location parameter. *Ann. Math. Stat.* **35**, 73–101 (1964).
99. Krieg, M. & Català Castro, F. Periodic obstacles regulate membrane tension propagation to enable localized mechanotransduction. *Zenodo* https://doi.org/10.5281/zenodo.15465212 (2025).

Acknowledgements

We would like to thank the NMSB laboratory for discussion, S. Ortiz-Vásquez (NMSB), M. Fernández-Campo (NMSB) and A. Farré (IMPETUX) for time-shared dual-trap characterization, F. Campelo (ICFO) for suggestions early in the work, F. Hoerndli (Colorado State) for comments on the draft and the *Caenorhabditis elegans* Center (CGC, supported by the National Institutes of Health, P40 OD010440) for the reagents. M.K. acknowledges financial support from the ERC (MechanoSystems, 715243), Human Frontiers Science Program (RGP021/2023), MCIN/AEI/10.13039/501100011033/ FEDER 'A way to make Europe' (PID2021-123812OB-I00, CNS2022-135906), 'Severo Ochoa' program for Centres of Excellence in R&D (CEX2019-000910-S), from Fundació Privada Cellex, Fundació Mir-Puig, and from Generalitat de Catalunya through the CERCA and Research program. ICFO is the recipient of the Severo Ochoa Award of Excellence of MINECO (Government of Spain). This work was supported in part by 1RF1DA055668-01, 5R01 MH139350 and the Air Force Office of Scientific Research Grant FA9550-18-1-0051 to P.R.

Author contributions

F.C.-C. and N.S.-C. performed the experiments. M.B.-Q. carried out the simulations. Data analysis was performed by F.C.-C., M.B.-Q., and M.K. The first draft of the manuscript was written by M.K. and F.C.-C. P.R. and M.K. supervised the project and acquired funding. All authors edited and revised the manuscript.

Competing interests

P.R. is a consultant for Simula Research Laboratory in Oslo, Norway, and receives income. The terms of this arrangement have been reviewed and approved by the University of California, San Diego, in accordance with its conflict-of-interest policies. The other authors declare no competing interests.

Additional information

Extended data is available for this paper at https://doi.org/10.1038/s41567-025-03037-x.

Supplementary information The online version contains supplementary material available at https://doi.org/10.1038/s41567-025-03037-x.

Correspondence and requests for materials should be addressed to Padmini Rangamani or Michael Krieg.

Peer review information *Nature Physics* thanks Eva Kreysing and Erik Schäffer for their contribution to the peer review of this work.

Reprints and permissions information is available at www.nature.com/reprints.

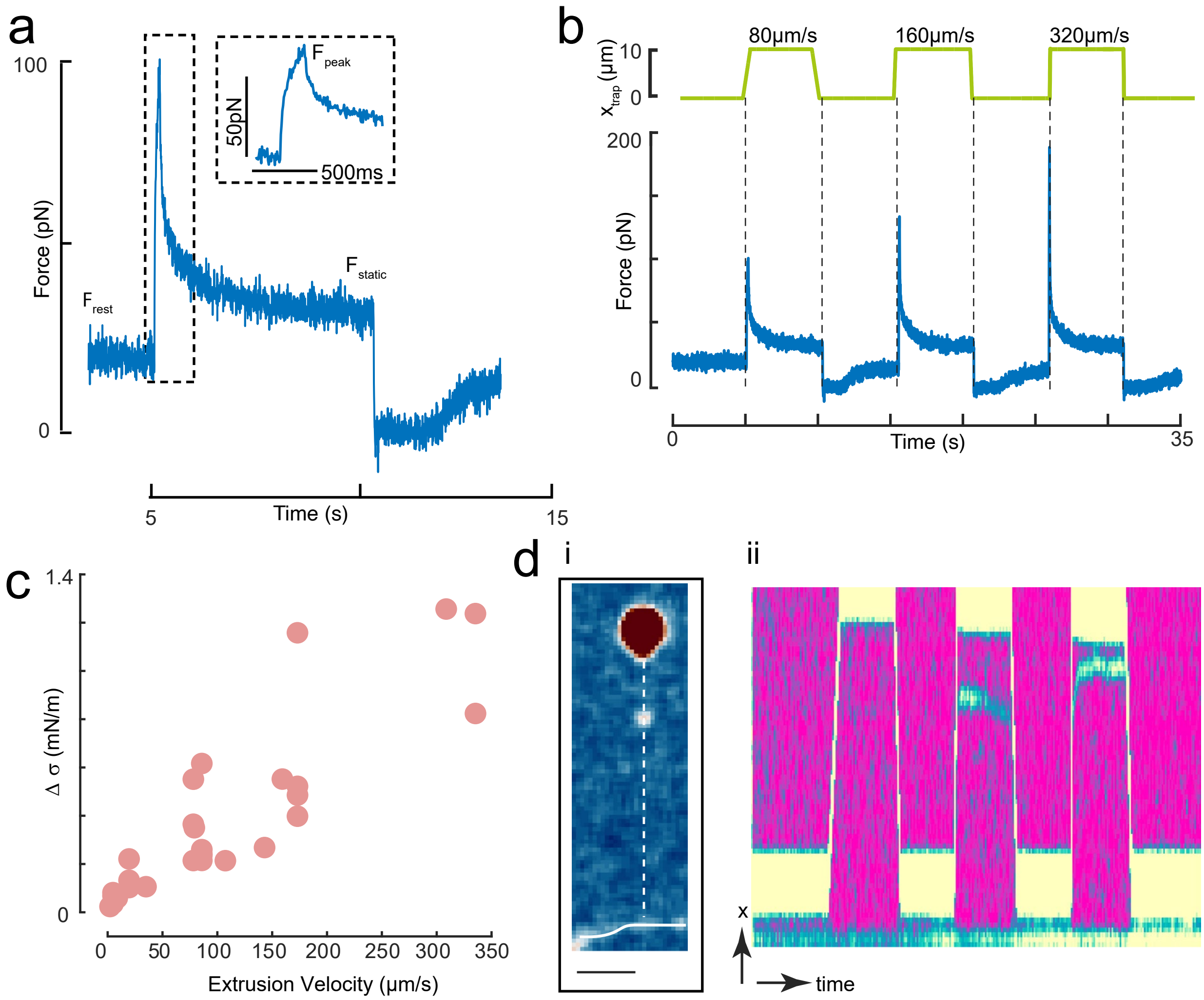

Extended Data Fig. 1 | Tether extrusion dynamics. a, Tether force profile upon extrusion. Inset shows the force peak during the extrusion event. Upon tether formation and before pulling, the non-zero force results from the baseline resting tension of the plasma membrane. After extrusion, force increases due to a tension gradient in the tether and once the trap stops moving, force decays to a static value until lipid flow into the tether equilibrates (tension gradient between tether and the neurite is zero, indicative for the steady state membrane tension. F_{rest}, F_{peak} and F_{static} indicate the feature used to extract the baseline, resting force, peak tether force, and steady-state plateau force, respectively. **b**, Consecutive tether extrusion events at the indicated retraction velocities. **c**, Peak membrane tension for DVA cells vs extrusion velocity. The increase in tension with increasing velocity depends on the viscosity of the membrane and the density of binders between the membrane and the cytoskeleton. The hydrodynamic force for a bead with R = 0.5 μm at a height h = 2 μm above the coverglass is $F_{\mathrm{drag}} = \frac{6\pi\eta(T)Rv}{(1-\frac{(9R)}{(16h)}-\frac{(R^3)}{(8h^3)})}$ where $\eta(T)$ is the temperature-dependent viscosity of water[94]. For the fastest pull v =3 20 μm/s, we obtain F_{drag} ~ 3.2pN, and therefore does not significantly contribute to the overall force measurements. **d**, Representative, false-colored plot of the traveling instability. (i) shows a snapshot of the bead tethered to the membrane. The tether is invisible but highlighted with a dotted line. The spherical protrusion travels toward the cell. Scale bar = 2 μm indicated below the micrograph. (ii) Kymograph, taken on the dotted line in the image above, shows the three consecutive extrusion events and the traveling instability along the tether. Scale bars: x=2 μm; time = 5 s.

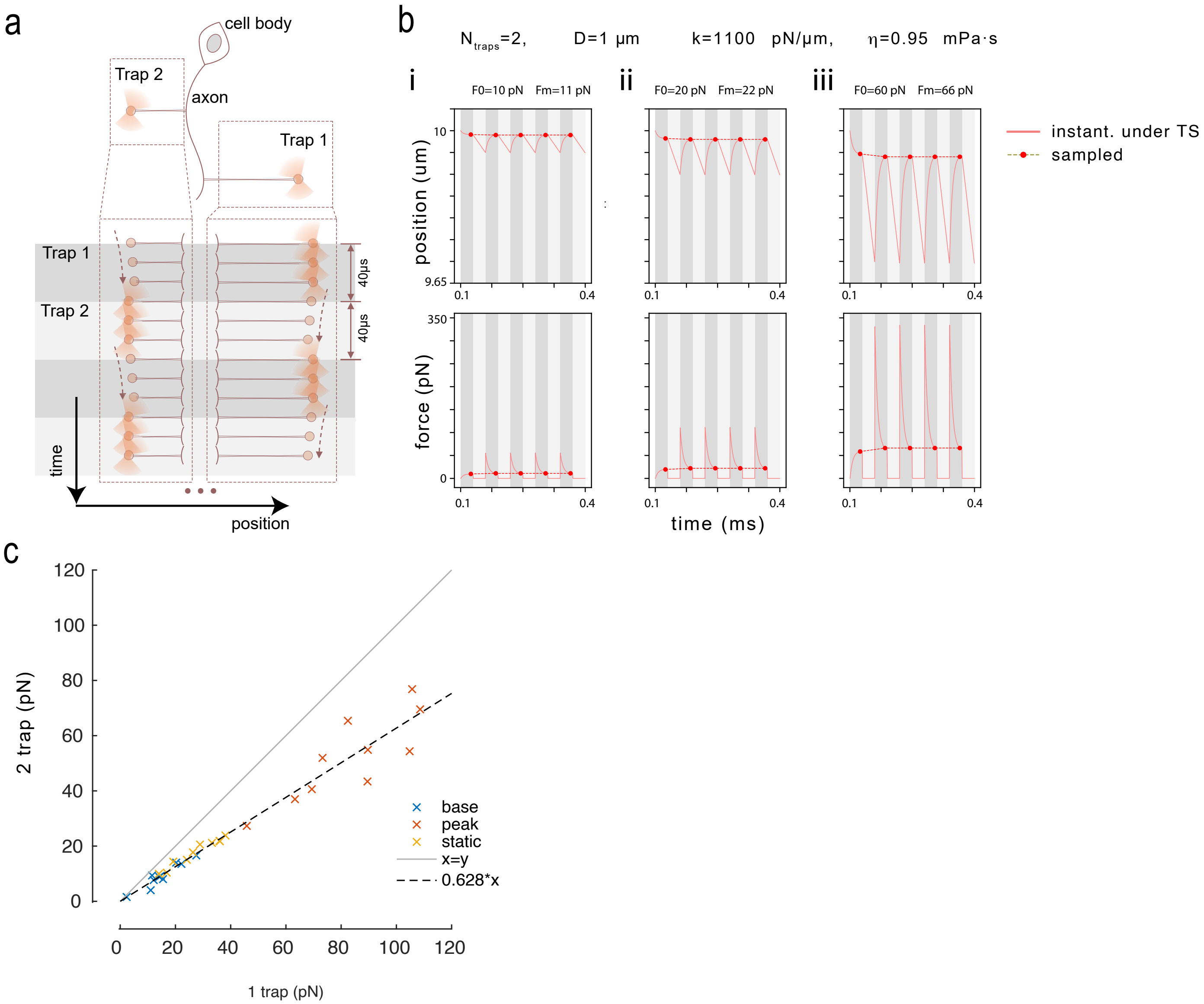

Extended Data Fig. 2 | Evaluating multiple trap time sharing dynamics. **a**, Schematic of the dual tether extrusion assay with time-shared optical tweezers, AOD-driven at 25 kHz. The laser spot resides in an interleaved sequence on each of the traps for $1/f_{TS} = 40\mu s$. Synchronously, the force sensor picks a datum, generating two force signals, those for traps 1 and 2, each of them sampled at 12.5 kHz. During the period half in which the laser spot resides on the other trap, the tethering force on bead 1 is not optically balanced, hence producing a slight bead creep towards the axon. **b**, Simulation of the instantaneous trajectory (top) and force (bottom) acting onto a bead for a tether applying a constant force of 10 pN (i), 20 pN (ii), and 60 pN (iii). In i-iii, the instantaneous trajectory is plotted in pink, sampled values at 25/2=12.5 kHz are represented by red dots connected by dashed lines. In the three simulations, the in silico force measurement overestimates the tether force by 10.2%. (See methods for details about the in silico modeling of the dual-trap time-sharing dynamics). (See Supplementary Text for details). **c**, We pulled 10 tethers from different cells and measured F_{rest}, F_{static} and F_{peak} during trapezoidal loading (Extended Data Fig. 8). Since the optical tweezers platform applies a 1/2 factor because a high-dissipation regime is assumed, experimental force measurement is underestimated by a factor of 0.63. See the Supplementary Information for discussion.

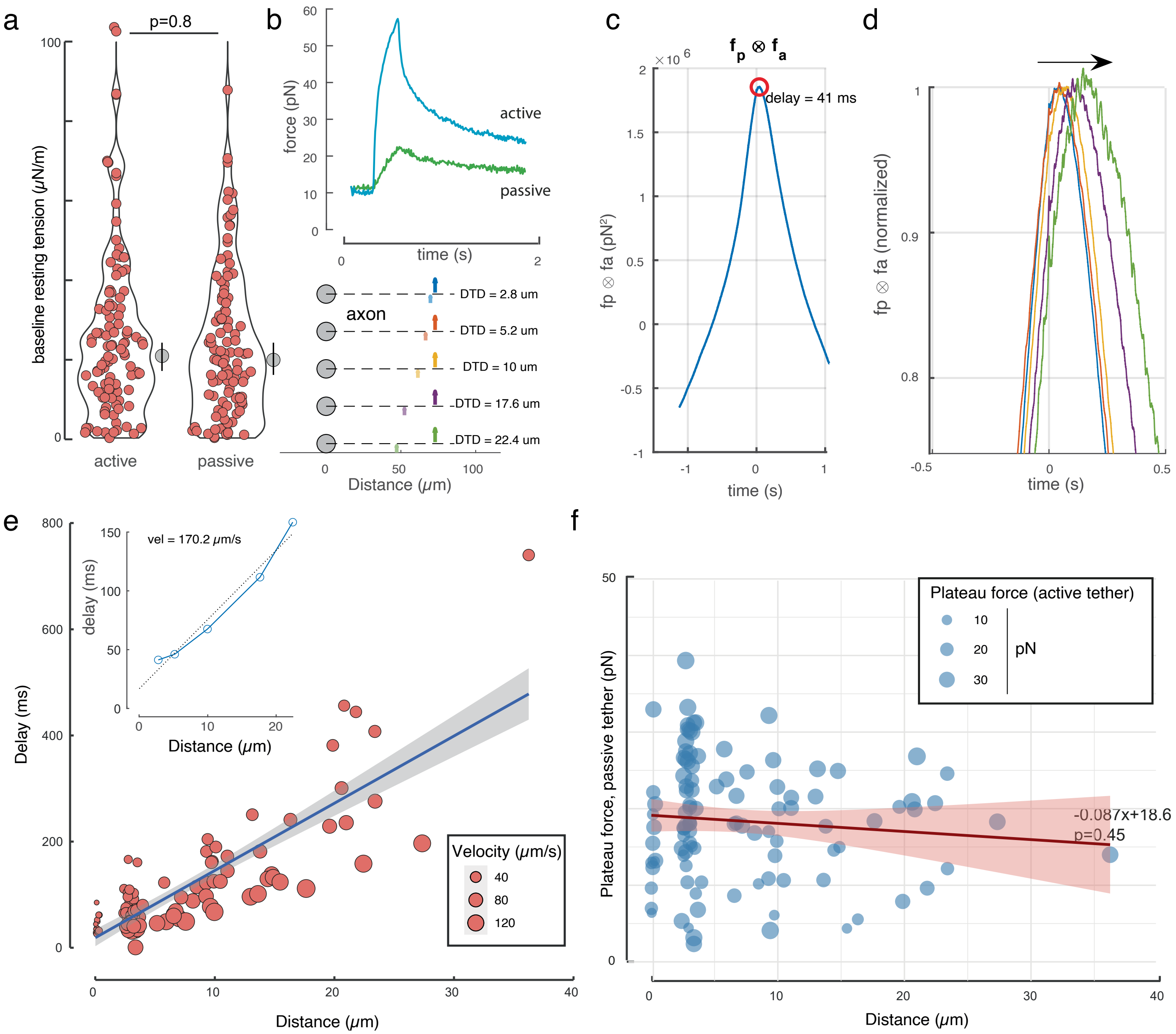

Extended Data Fig. 3 | Properties of the dual tether extrusion dynamics. **a**, Violin plot of the baseline resting tension extracted from the active and the passive tether of wildtype TRNs. *P* value above the horizontal line determined from a two-sided KS test. Black circle with the vertical bar indicates the median and its 95% confidence interval, respectively. **b-d**, Procedure used to determine the time delay (or lag) between the active and the passive tether. (**b**) Representative force-time traces of the active (blue) and the passive (green) tether. The sketch indicates the position of the two tethers (active, big arrow; passive, small arrow) extruded from the axon (dashed line) with respect to the cell body (grey circle; DTD, dual tether distance), (**c**) Representative cross correlation of the active (f_a) and the passive (f_p) tether with the time delay indicated close to the peak. Matlab function *xcorr* was used for this calculus. (**d**) Visualization of the increase in time lag with increase in distance. Curves are colored according to the sketch in b. **e**, Plot of the delay between the two force peaks and the tether separation distance. Size of the dots corresponds to the velocity (μm/s). Blue line is the linear regression with the shadow as the 95% confidence interval. Inset shows a representative example of different pulling events of the same tether at various distances. **f**, Plot of the plateau force of the passive tether with increasing distance to the active tether. The plateau force of the active tether is indicated as circle size. The slope of the linear regression and the *P* value of significance is indicated next to the blue line (fit ± SEM).

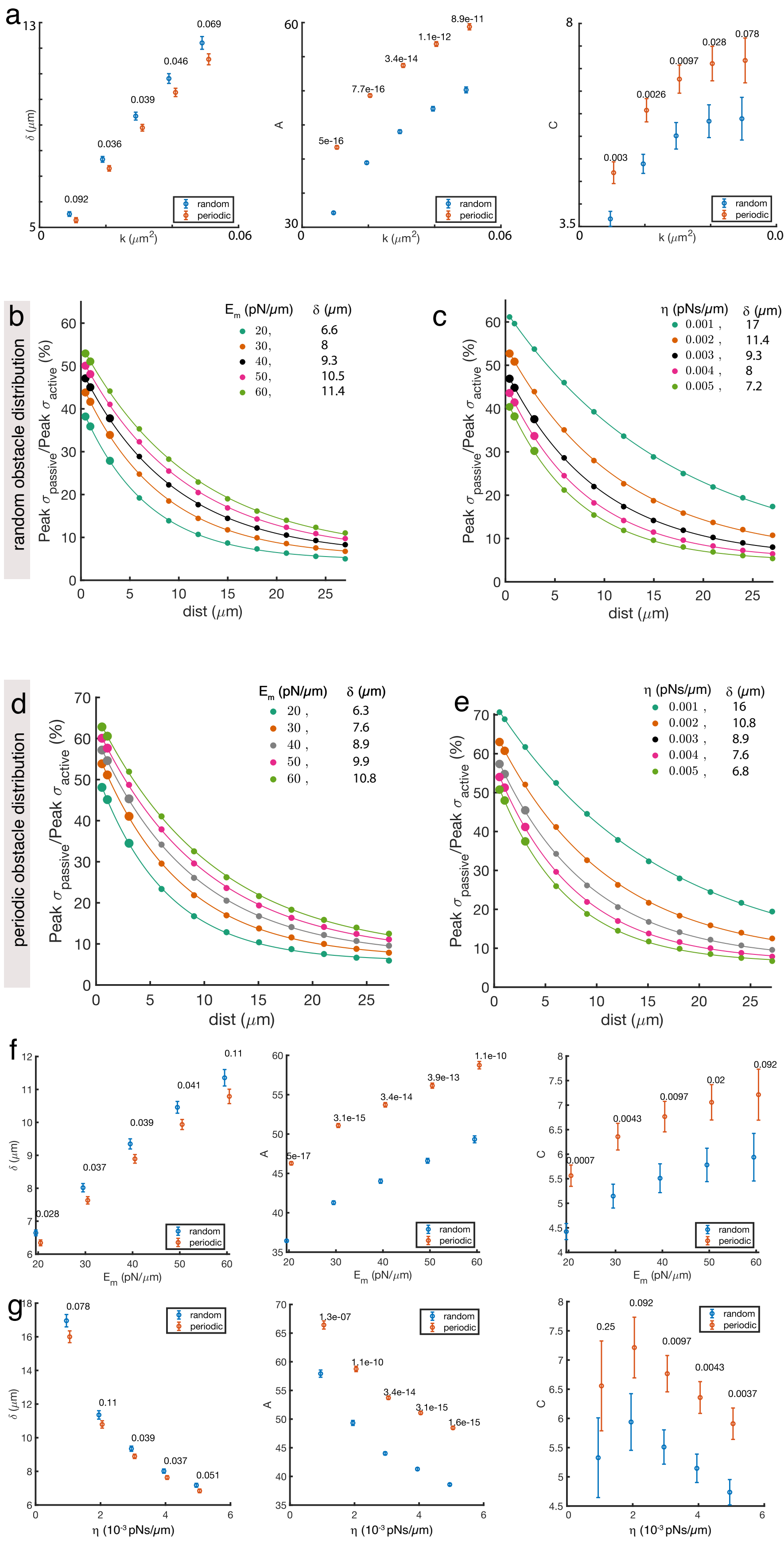

Extended Data Fig. 4 | See next page for caption.

Extended Data Fig. 4 | Theoretical model for tension propagation. a, Plot of the characteristic length scale δ, amplitude A, and the offset C, ± their standard error, respectively, obtained from exponential fits with offset to simulations with random and periodic obstacle arrangements, plotted as a function of permeability k. P values above the points indicate the outcome of the statistical test comparing the fit parameters as described in the methods. **b**, **c**, Change in membrane tension measured at the *passive* lipid nanotube for increasing distances normalized to the active, pulling site, with different (**b**) membrane expansion modulus and (**c**) viscosities. Circle size corresponds to the amount of tension in the passive tether in the simulation (small $0 < \sigma \leq 3$ pN/μm, medium $3 < \sigma \leq 6$pN/μm, and big $6 < \sigma \leq 9$pN/μm). Lines are weighted exponential fits to the *passive* tether. Black color represents the control condition. **d**, **e**, Change in membrane tension propagation using the periodic configuration for different parameters (**d**) membrane expansion modulus and (**e**) viscosities. Note that k corresponds to the mean value of the permeability along the axon taking $k_+ = 1.5k$ and $k\text{-}=(3k\text{-}k_+)/2$. Grey color corresponds to the control condition. **f**, Plot of the characteristic length scale δ, amplitude A, and the offset C, ± their standard error, respectively, obtained from an exponential fits with an offset to simulations with random and periodic obstacle arrangements, plotted as a function of membrane elasticity E_m. P values above the points indicate the outcome of the two-tailed t-test comparing the fit parameters. **g**, Plot of the characteristic length scale δ, amplitude A, and the offset C, ± their standard error, respectively, obtained from exponential fits with offset to simulations with random and periodic obstacle arrangements, plotted as a function of membrane viscosity η. P values above the points indicate the outcome of the two-tailed t-test comparing the fit parameters as described in the methods.

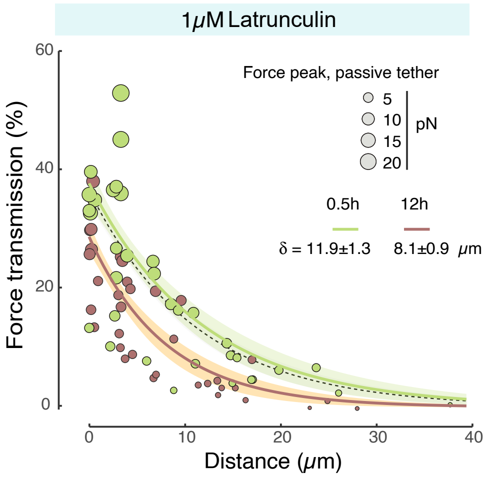

Extended Data Fig. 5 | Tension propagation with different LatA concentrations. Change in membrane tension measured at the *passive* lipid nanotube for increasing distances normalized to the *active*, pulling site, with different incubation times of Latrunculin A. The size of the points corresponds to the absolute transmitted force at the passive tether. Exponential fit is weighted by the transmitted force, *δ* indicates characteristic length scale of tension propagation. Red points indicate values derived from over night incubation, green points from 30 min incubation with 1 μM LatA. The dotted black line indicates the fit derived from control data (as shown in Fig. 1d). Solid lines indicate a fit to an exponential decay as described in the methods and the error band is the 95% confidence interval of the fit as described in the methods.

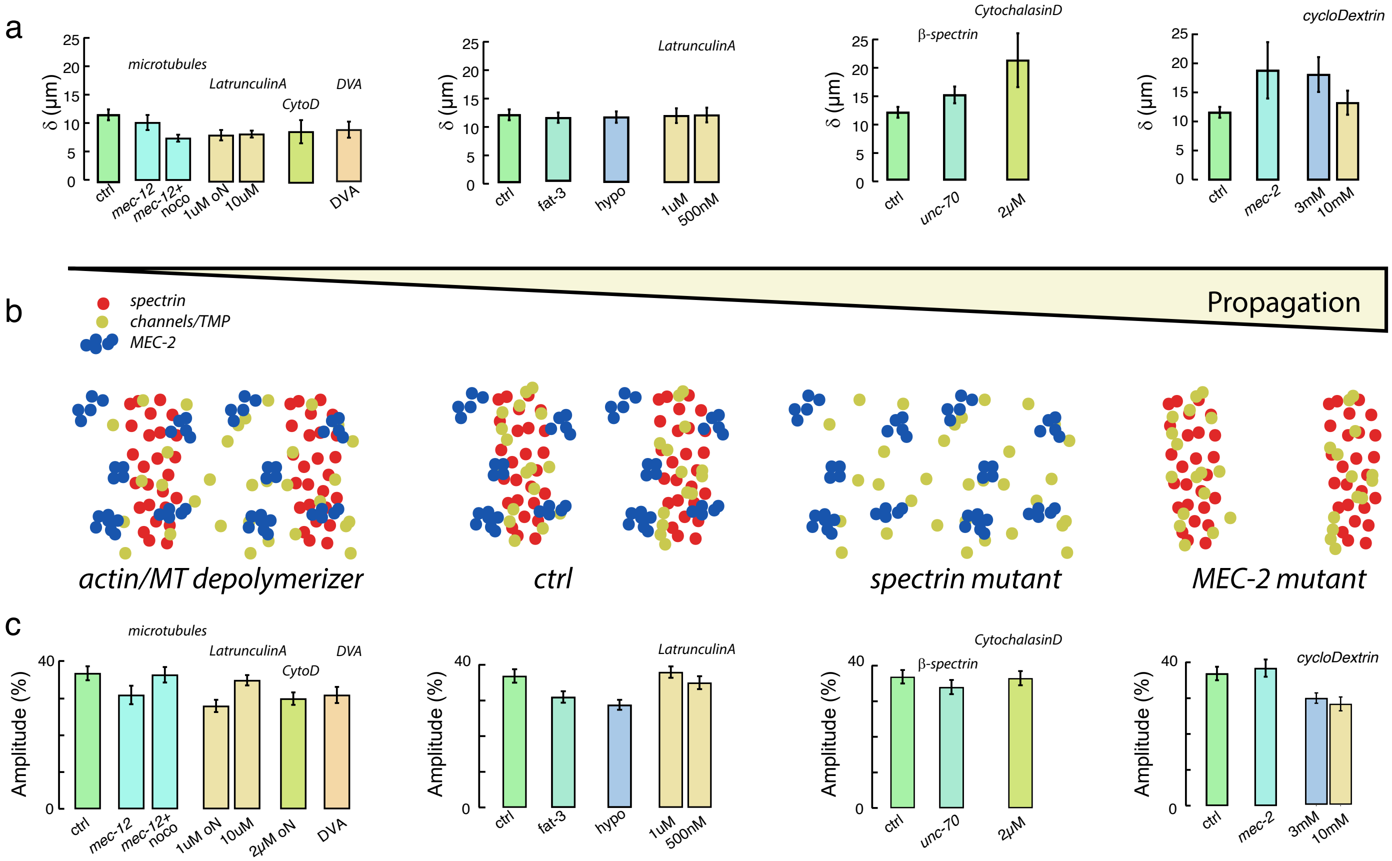

Extended Data Fig. 6 | Summary of the treatments changing tension propagation. a, Fit parameter *δ* describing the characteristic length scale of the tension propagation derived from the dual tether pulling experiment acquired under the described perturbation. Error bars indicate the standard errors of the fit, obtained using a robust Levenberg-Marquardt procedure with Huber weights. **b**, Schematic of the outcome on the arrangement of obstacles impeding tension propagation. Different mechanism can lead to the same outcome, for example removal of the periodic arrangement as well as obstacle clustering. **c**, Fit parameter A describing the amplitude of the exponential fit, indicating the percentage of transmitted force when the distance of the two traps approached each other. Error bars indicate the standard errors of the fit, obtained using a robust Levenberg-Marquardt procedure with Huber weights. Numbers and replicates indicated in Table S1.

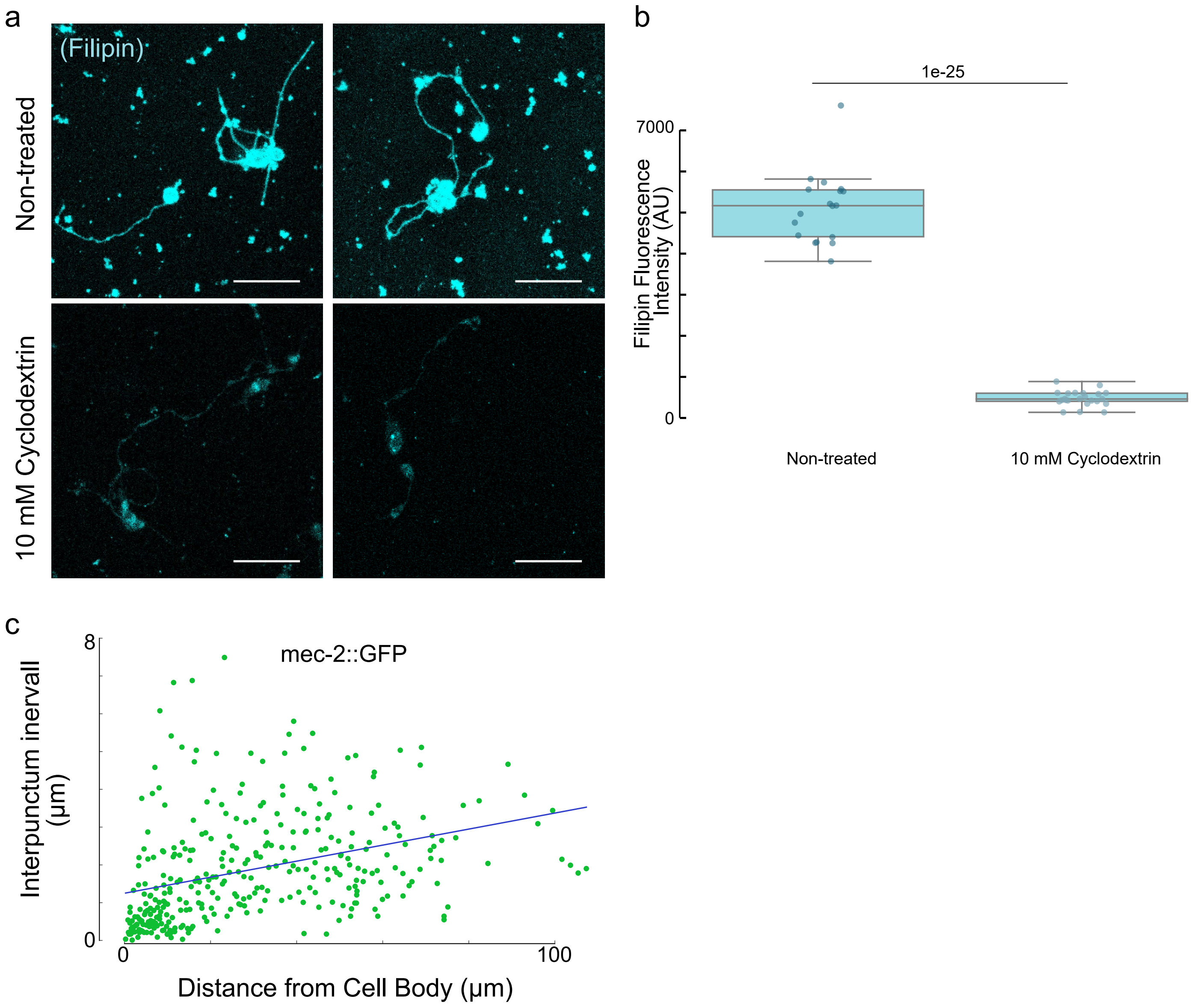

Extended Data Fig. 7 | CycloDextrin treatment reduces choleresterol content. **a**, Representative pictures of control and mbCD (10mM) treated TRNs stained with filipin to visualize cholesterol. Scalebar = 10 μm. **b**, Box plot and individual data points of the filipin fluorescent intensity acquired from different control (N=18) and mbCD-treated (N=23) cells from two independent experiments. Box plots indicate the median (center line), interquartile range (box limits: 25th-75th percentiles), and whiskers extending to the most extreme values within 1.5 × IQR. *P* value derived from a two-sided t-test. **c**, Distribution of MEC-2 interpunctum intervall along the length of the neurites of cultured TRNs. Cell body is to the left.

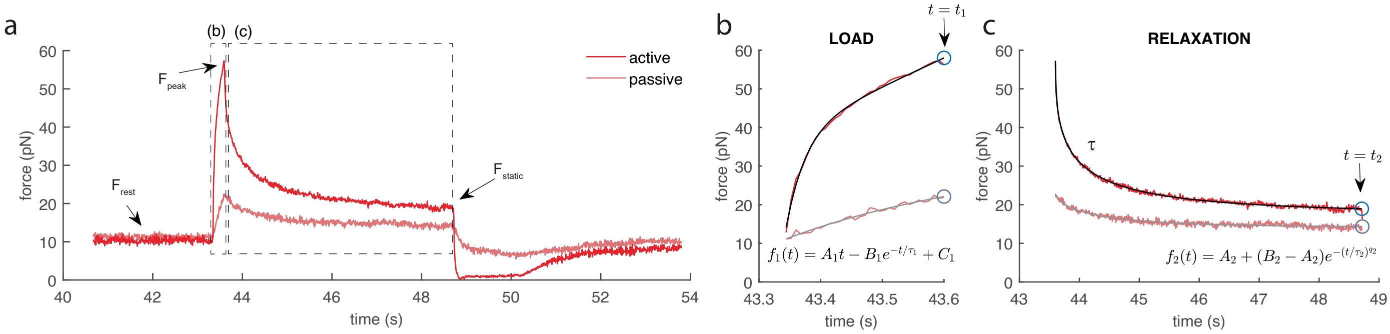

Extended Data Fig. 8 | Methods: Data processing. Graphical representation of the fitting procedure to extract features from the force curves such as F_{rest}, F_{peak} and F_{static}. **a**, Representative active/passive tether pair. Corresponds to dt52cc in the raw data file folder on Zenodo[99]. **b**, Close up onto the inset (**b**) in (**a**) with the corresponding fit shown as black and grey solid line. The fitting function is indicated below. **c**, Close up onto the inset (**c**) in (**a**) with the corresponding fit shown as black and grey solid line. The fitting function is indicated below. See methods for details. τ_2 is the decay constant extracted from the stretched exponential.

nature portfolio

Corresponding author(s): Krieg, Michael

Last updated by author(s): Aug 8, 2025

Reporting Summary

Nature Portfolio wishes to improve the reproducibility of the work that we publish. This form provides structure for consistency and transparency in reporting. For further information on Nature Portfolio policies, see our Editorial Policies and the Editorial Policy Checklist.

Statistics

For all statistical analyses, confirm that the following items are present in the figure legend, table legend, main text, or Methods section.

n/a	Confirmed	
☐	☒	The exact sample size (*n*) for each experimental group/condition, given as a discrete number and unit of measurement
☒	☐	A statement on whether measurements were taken from distinct samples or whether the same sample was measured repeatedly
☒	☐	The statistical test(s) used AND whether they are one- or two-sided *Only common tests should be described solely by name; describe more complex techniques in the Methods section.*
☐	☒	A description of all covariates tested
☐	☒	A description of any assumptions or corrections, such as tests of normality and adjustment for multiple comparisons
☐	☒	A full description of the statistical parameters including central tendency (e.g. means) or other basic estimates (e.g. regression coefficient) AND variation (e.g. standard deviation) or associated estimates of uncertainty (e.g. confidence intervals)
☐	☒	For null hypothesis testing, the test statistic (e.g. *F*, *t*, *r*) with confidence intervals, effect sizes, degrees of freedom and *P* value noted *Give P values as exact values whenever suitable.*
☒	☐	For Bayesian analysis, information on the choice of priors and Markov chain Monte Carlo settings
☒	☐	For hierarchical and complex designs, identification of the appropriate level for tests and full reporting of outcomes
☒	☐	Estimates of effect sizes (e.g. Cohen's *d*, Pearson's *r*), indicating how they were calculated

Our web collection on statistics for biologists contains articles on many of the points above.

Software and code

Policy information about availability of computer code

Data collection	All data collection software (Andor Fusion imaging software, Impetux SENSOCELL LightACE optical tweezer software) is described in detail in the methods section for each experiment. No custom acquisition software was used. Confocal images were acquired with Andor FusionSoftware.
Data analysis	Optical Tweezer data was analyzed using custom-written Matlab scripts (Version 2021). All custom computer scripts are available upon request. No specialized standalone software was developed as part of this manuscript.

For manuscripts utilizing custom algorithms or software that are central to the research but not yet described in published literature, software must be made available to editors and reviewers. We strongly encourage code deposition in a community repository (e.g. GitHub). See the Nature Portfolio guidelines for submitting code & software for further information.

Data

Policy information about availability of data

All manuscripts must include a data availability statement. This statement should provide the following information, where applicable:

- Accession codes, unique identifiers, or web links for publicly available datasets
- A description of any restrictions on data availability
- For clinical datasets or third party data, please ensure that the statement adheres to our policy

All data is available in the manuscript and the supplementary materials.

Research involving human participants, their data, or biological material

Policy information about studies with human participants or human data. See also policy information about sex, gender (identity/presentation), and sexual orientation and race, ethnicity and racism.

Reporting on sex and gender	Does not apply
Reporting on race, ethnicity, or other socially relevant groupings	Does not apply
Population characteristics	Does not apply
Recruitment	Does not apply
Ethics oversight	Does not apply

Note that full information on the approval of the study protocol must also be provided in the manuscript.

Field-specific reporting

Please select the one below that is the best fit for your research. If you are not sure, read the appropriate sections before making your selection.

☒ Life sciences ☐ Behavioural & social sciences ☐ Ecological, evolutionary & environmental sciences

For a reference copy of the document with all sections, see nature.com/documents/nr-reporting-summary-flat.pdf

Life sciences study design

All studies must disclose on these points even when the disclosure is negative.

Sample size	No a priori method or power analysis was applied to determine an optimal sample size.
Data exclusions	No statistical outliers have been identified. Only cells that were visually confirmed `healthy' were used for analysis and data acquisition.
Replication	All experimental conditions contain data from different cell cultures and confirmed replicability.
Randomization	Whenever possible, experimental conditions were randomized to avoid history effects in the optical tweezer mechanics experiments.
Blinding	Investigators in this study were not blinded during data collection nor image and data processing and analysis.

Reporting for specific materials, systems and methods

We require information from authors about some types of materials, experimental systems and methods used in many studies. Here, indicate whether each material, system or method listed is relevant to your study. If you are not sure if a list item applies to your research, read the appropriate section before selecting a response.

Materials & experimental systems

n/a	Involved in the study	
☒	☐	Antibodies
☒	☐	Eukaryotic cell lines
☒	☐	Palaeontology and archaeology
☐	☒	Animals and other organisms
☒	☐	Clinical data
☒	☐	Dual use research of concern
☒	☐	Plants

Methods

n/a	Involved in the study	
☒	☐	ChIP-seq
☒	☐	Flow cytometry
☒	☐	MRI-based neuroimaging

Animals and other research organisms

Policy information about studies involving animals; ARRIVE guidelines recommended for reporting animal research, and Sex and Gender in Research

Laboratory animals	Primary cell cultures from Caenorhabditis elegans embryos (wildtype N2 and mutants listed in the manuscript).
Wild animals	Does not apply
Reporting on sex	Cell were extracted from a mixed population of hermaphrodite and male animals, cultures thus likely contain neurons of both sexes. Due to the bulk preparation, a separation is impossible.
Field-collected samples	Does not apply
Ethics oversight	Nematodes are exempt from ethics approval.

Note that full information on the approval of the study protocol must also be provided in the manuscript.

Plants

Seed stocks	Does not apply
Novel plant genotypes	Does not apply
Authentication	Does not apply